REVIEW

Hyperspectral remote sensing in lithological mapping, mineral exploration, and environmental geology: an updated review

Sima Peyghambari* **and Yun Zhang**
University of New Brunswick, Geodesy and Geomatic Engineering Department, Fredericton, New Brunswick, Canada

Abstract. Hyperspectral imaging has been used in a variety of geological applications since its advent in the 1970s. In the last few decades, different techniques have been developed by geologists to analyze hyperspectral data in order to quantitatively extract geological information from the high-spectral-resolution remote sensing images. We attempt to review and update various steps of the techniques used in geological information extraction, such as lithological and mineralogical mapping, ore exploration, and environmental geology. The steps include atmospheric correction, dimensionality processing, endmember extraction, and image classification. It is identified that per-pixel and subpixel image classifiers can generate accurate alteration mineral maps. Producing geological maps of different surface materials including minerals and rocks is one of the most important geological applications. The hyperspectral images classification methods demonstrate the potential for being used as a main tool in the mining industry and environmental geology. To exemplify the potential, we also include a few case studies of different geological applications. [DOI: 10.1117/1.JRS.15.031501]

Keywords: hyperspectral remote sensing; geological applications; mineral spectra; lithological mapping; ore exploration; environmental geology.

Paper 210082V received Mar. 10, 2021; accepted for publication Jun. 25, 2021; published online Jul. 14, 2021.

1 Introduction

High-spectral resolution (hyperspectral) remote sensing has been used for Earth observation since the advent of imaging spectrometer systems.[1] Hyperspectral sensors can acquire images in 100 to 200 contiguous spectral bands, to provide a unique combination of spatially and spectrally contiguous images.[2] Thanks to its ability to capture unique spectral signatures of the surface material, hyperspectral imaging has been used in various Earth observation applications including earth science, forestry, geography, agriculture, hydrography, atmosphere, climate change monitoring, military, security and law enforcement.[3]

In earth science, geologic remote scientists have also utilized the advantages of hyperspectral imaging in different geological applications, such as mineral industry, water quality determination, oil, and gas industries. They conducted hyperspectral imaging at various scales from close range imaging including rock samples,[4] cores,[5] and outcrop scanning[6] to airborne and spaceborne acquisition.[7,8]

There are several review papers on the topic of geologic hyperspectral remote sensing, including applications of hyperspectral remote sensing in geology,[9] multi- and hyperspectral geologic remote sensing,[7] mineral mapping using hyperspectral data,[10] spectral processing methods for geological remote sensing,[11] hyperspectral remote sensing and geological applications,[12] and hyperspectral remote sensing for mineral exploration.[13]

However, an up-to-date review that covers the various components of using hyperspectral remote sensing for geological applications is needed for future research. This paper attempts to fill the gap by providing an updated review on hyperspectral missions, spectral properties

*Address all correspondence to Sima Peyghambari, sima.peyghambari@unb.ca

of diagnostic minerals, and various techniques for geologic information extraction from spaceborne/airborne hyperspectral images. The techniques include preprocessing, dimension reduction, endmember retrieval, and important image classification methods.

2 Hyperspectral Sensors

Over the last decades, airborne hyperspectral sensors including AVIRIS, HYDICE, DAIS, and HyMAP overwhelmed the hyperspectral imaging. However, using spaceborne hyperspectral sensors makes this technology more available for researchers. The launch of NASA's EO-1 Hyperion sensor with 242 spectral bands in 0.4 to 2.5 μm made the new beginning in hyperspectral remote sensing. Several further spaceborne hyperspectral sensors have also launched in the target of scientific research and land imaging, Earth observation, and natural resources and atmosphere such as Tiangong-1, EnMAP, and PRISMA. However, there are plans for future development of hyperspectral satellite sensors including HypXIM and HyspIRI. Table 1 represents some of the main hyperspectral missions with the target of Earth observation. Although most of the spaceborne hyperspectral imageries (HSIs) have moderate spatial resolution (30 m) (Table 1), some of the hyperspectral sensors such as PRISMA and forthcoming HypXIM use the advantages of panchromatic sensors with the resolution of 5 and 2 m, respectively.

3 Spectral Properties of Different Minerals

Hyperspectral imaging data in the 0.4- to 2.5-μm visible- and near-infrared (VNIR) and shortwave infrared (SWIR) spectral range are diagnostic in mineralogic and lithological mapping in different climate and tectonic settings.[12] Due to distinct spectral absorption feature, many minerals and rocks are distinguishable through their spectral patterns.[9,14,15] Figure 1 shows the accuracy of different minerals in various wavelengths including VNIR, SWIR, and long-wave infrared (LWIR) or thermal infrared (TIR).[16] Therefore, hydrothermally altered and unaltered rocks can be discriminated and mapped via the diagnostic signatures in the VNIR and SWIR regions.[17]

Iron oxides and hydroxides including hematite, jarosite, limonite, and goethite show distinct spectral absorption in VNIR from 0.4 to 1.1 μm. Iron oxides and hydroxide minerals are mostly developed during the hydrothermal alteration processes associated with different ore bodies such as porphyry copper deposits (PCDs).[17]

Hydroxyl-bearing minerals such as phyllosilicate, clay minerals, sulfate, and carbonate groups show distinct spectral absorption in SWIR radiation region. Different minerals including Al-Si-(OH) and Mg-Si-(OH)-bearing minerals such as clay minerals, talc, and chlorite, and Ca-Al-Si-(OH)-bearing sorosilicate minerals such as epidote and OH-bearing sulfates such as alunite and gypsum, and carbonates have diagnostic spectral characteristics in SWIR region. Due to internal structures of the quartz mineral, it shows absorption signature around 8.3 to 9.1, which belongs to TIR region.[18]

Spectral signatures of some hydrothermal minerals are presented in Figs. 2(a) and 2(b). Figure 2(a) reflects the absorption features of the Al-O-H, Mg-O-H minerals, alunite, and carbonates in SWIR region, whereas Figure 2(b) shows the spectra features of the Fe oxides and hydroxides.[19] These minerals mostly associated with different hydrothermal alterations around various ore deposits. Therefore, spectral feature of the minerals, which is one of the most important aspects of hyperspectral remote sensing, can be used for lithologic and mineral mapping as well as ore exploration. Figure 3 shows the spatial distribution of different minerals with diagnostic spectral properties from VNIR and SWIR AVIRIS hyperspectral data over Cuprite, Nevada.

There are several well-characterized spectral repositories of minerals and rocks such as United States Geological Survey (USGS), John Hopkins University (JHU) and Jet Propulsion Laboratory (JPL), Emission and Reflectance Spectral Library (EARSL), and National Mineral Collection (NMC) spectral library. The USGS provided spectral library of minerals and rocks from 0.35 to 2.5 μm regions. The JHU spectral library covers from 2 to 25 μm regions.[20] NASA JPL spectral library includes minerals with spectral features from 0.4 to 2.5 μm. The Council of

Table 1 The specific spectral characteristics of various hyperspectral missions.

No.	Sensor	Satellites/ platform	Launch time	Organizations	Number of bands	Spectral range (μm)	Spectral resolution (nm)	GSD (m)	Swath width (km)	Spectral imaging techniques	Application
1	Hyperion	EO-1	2000	NASA	19 to 62	0.4 to 2.5	10	30	7.7	Grating and pushbroom	Earth observation; mining, geology, forestry, land, and area mapping
2	CHRIS	PROBA	2001	ESA	19 to 62	0.4 to 1.0	1.25 to 11	25 to 50	13	Prism, pushbroom, and multi-viewing	Land and water related applications and aerosol measurements
3	MERIS	ENVISAT	2001	ESA	520 (transmit)	0.39 to 1.04	1.25	300	1150	Grating, pushbroom, and onboard band width selection	Ocean observation
4	FTHSI	HJ-1A	2008	NCDR/SEPA	115	0.45 to 0.95	4	100	50	Fourier interferometer	Earth observation
5	TianGong-1	Shenzhou-8	2011	Chinese Academy of Science and Physics	128	0.40 to 0.25	10 VNIR 23 SWIR	30	10	Pushbroom	Scientific research and land imaging
6	AHSI	Gaofen-5	2018	Shanghai Institute	330	0.40 to 2.50	5 VNIR 10 SWIR	30	60	Grating and pushbroom	Earth observation
7	HysIS	IMS-2	2018	COSPAR ID	256	0.40 to 2.40	10	30	30	Dispersive (?)	Agriculture, forestry, and geography
8	PRISMA	PRISMA	2019	ASI	237	0.40 to 2.51	12	30	30	Prism and pushbroom	Natural resources and atmosphere
9	HISUI	ALOS-3	2019	METI	185	0.40 to 2.50	10 VNIR 12.5 SWIR	30	30	Grating and pushbroom	Energy and vegetation monitoring
10	HyspIRI	HyspIRI	2020	JPL, NASA	>200	0.38 to 0.25	10	60	145	Pushbroom	Volcanic, vegetation, soil, and exploration
11	EnMAP	German HS	2021	GFZ/DLR	244	0.42 to 2.50	5 and 10	30	30	Prism and pushbroom	Earth observation
12	HypXIM	HypXIM	2023	CNES	214	0.4 to 0.25	10	8	15	Pushbroom	Soil, urban, and coastal biodiversity

Type	Silicate structure	Mineral group	Example	VNIR response	SWIR response	LWIR response
Silicates	Inosilicates	Amphibole	Actinolite	Non-diagnostic	Good	Moderate
		Pyroxene	Diopside	Good	Moderate	Good
	Cyclosilicates	Tourmaline	Elbaite	Non-diagnostic	Good	Moderate
	Nesosilicates	Garnet	Grossular	Moderate	Non-diagnostic	Good
		Olivine	Forsterite	Good	Non-diagnostic	Good
	Sorosilicates	Epidote	Epidote	Non-diagnostic	Good	Moderate
	Phyllosilicates	Mica	Muscovite	Non-diagnostic	Good	Moderate
		Chlorite	Clinochlore	Non-diagnostic	Good	Moderate
		Clay minerals	Illite	Non-diagnostic	Good	Moderate
			Kaolinite	Non-diagnostic	Good	Moderate
	Tectosilicates	Feldspar	Orthoclase	Non-diagnostic	Non-diagnostic	Good
			Albite	Non-diagnostic	Non-diagnostic	Good
		Silica	Quartz	Non-diagnostic	Non-diagnostic	Good
Non-silicates	Carbonates	Calcite	Calcite	Non-diagnostic	Moderate	Good
		Dolomite	Dolomite	Non-diagnostic	Moderate	Good
	Hydroxides		Gibbsite	Non-diagnostic	Good	Moderate
	Sulphates	Alunite	Alunite	Moderate	Good	Moderate
			Gypsum	Non-diagnostic	Good	Good
	Borates		Borax	Non-diagnostic	Moderate	TBD
	Halides	Chlorides	Halite	Non-diagnostic	TBD	TBD
	Phosphates	Apatite	Apatite	Moderate	Non-diagnostic	Good
	Hydrocarbons		Bitumen	TDB	Moderate	TBD
	Oxides	Hematite	Hematite	Good	Non-diagnostic	Non-diagnostic
		Spinel	Chromite	Non-diagnostic	Non-diagnostic	Non-diagnostic
	Sulphides		Pyrite	Non-diagnostic	Non-diagnostic	Non-diagnostic

Fig. 1 Qualitative accuracy of spectral analyses in VNIR, SWIR, and LWIR ranges.[16]

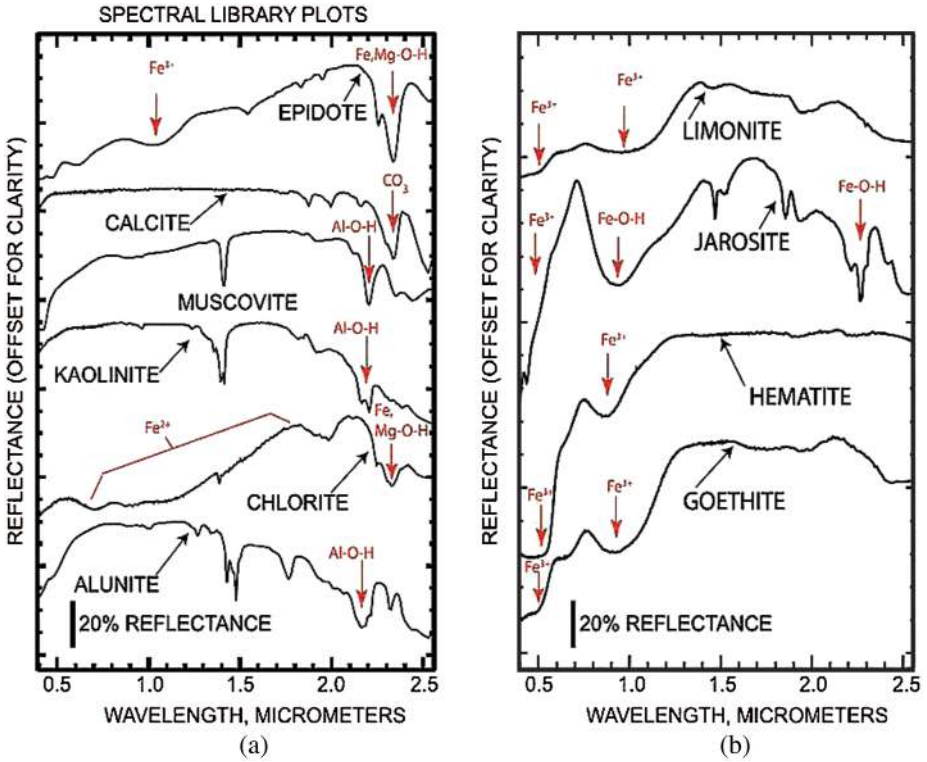

Fig. 2 Laboratory spectral features of different hydrothermal minerals including (a) clay minerals and (b) iron oxides.[18]

Industrial Research Organization of Australia has developed the EARSL of different minerals. The NMC produced by Geological Survey of Canada contains more than 100,000 minerals.[21]

Although spectral libraries of different minerals produced in laboratories have been widely used in mineral and rock identifications, some natural heterogenies existed in various minerals and associated spectral mixing possibly still have unwanted effects on the image processing results.[22,23] Field spectroscopy is evolving as a robust technique to overcome this issue specially

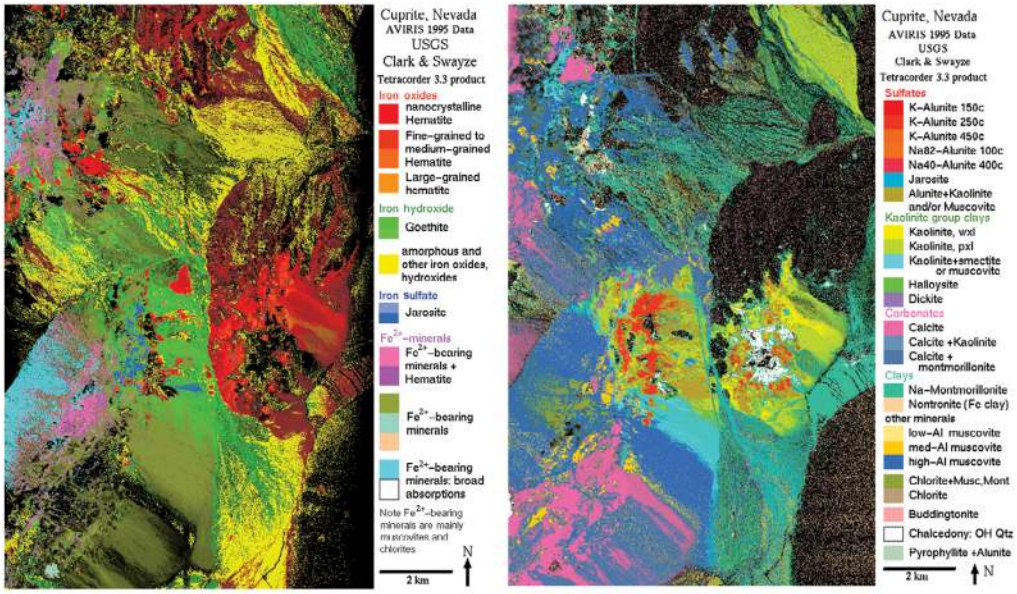

Fig. 3 Mapping results from the analysis of (a) VNIR and (b) SWIR AVIRIS hyperspectral data from Cuprite area, Nevada.[15]

in mineral mapping and ore exploration. Hyperspectral data from cores provide information about different mineral grades in ore exploration.[10] Combination of field spectroscopy with spaceborne/airborne hyperspectral images can get reliable results from image processing.

4 Hyperspectral Data Processing

4.1 *Hyperspectral Image Preprocessing*

Different levels of preprocessing are available to correct the original hyperspectral images including geometric and atmospheric correction (ATCOR). Bad characteristics of an image that have been caused by the sensor can be removed by geometric or sensor error correction techniques. These errors involve stripes and other noise type distortions.[24,25] For example, several vertical lines with no information can be produced by detectors in Hyperion sensor. The information from these areas can be covered by replacing their pixel values with the average pixel values of their neighboring pixels.[25]

Due to scattering and absorption of solar radiation and spectra by atmospheric gases and aerosols, the hyperspectral images have atmospheric effects. These atmospheric effects must be removed in order to use hyperspectral data for quantitative remote sensing.[26] ATCOR methods have evolved through the years so that they can be categorized as scene-based empirical approaches and radiative transfer model (RTM)-based approaches.[25–28] Several scene-based empirical approaches were developed to correct the atmospheric effects on the hyperspectral images. Kruse[23] computed the average spectrum of a scene by internal average spectrum of a scene. Then the corresponding spectrum of any pixel is divided by the average spectrum to get relative reflectance spectrum for each pixel. This method was mostly applied for areas without any vegetation. Roberts et al.[29] introduced flat field correction approach. They normalized the input image to an assumed area with neutral spectrally reflectance (with flat topographic and spectral feature). The empirical line approach[30] uses field reflectance spectra for bright and dark targets to linearly correlate the raw input imaging spectrometer data. Reinersman et al.[31] developed empirical "cloud shadow" method for ATCOR over the darker water surfaces. The quick ATCOR approach[32] is developed to remove atmospheric effects from multispectral and hyperspectral images in VNIR and SWIR bands. This approach drives atmospheric compensation factor directly from imaging spectrometer data.

RTMs are physically based codes that try to simulate the transfer process of an electromagnetic wave in the atmosphere.[33] They need field-based measurement of the atmosphere conditions at the time of image attainment and produce apparent reflectance or scaled surface reflectance.[25,34] There are several RTM-based algorithms to model the ATCOR. Atmospheric removal algorithm was developed by Gao et al.[35] This model performed to retrieve ground reflectance spectra from hyperspectral data by a theoretical modeling technique. It simulates the absorption and scattering effects of gases and aerosols existing in the atmosphere. ATCOR developed by Richter[36] includes a large database of ATCOR functions. It covers a wide range of atmospheric conditions. Kruse[27] developed ATCOR now algorithm, which is model-based ATCOR software using MODTRAN-4 code to reduce atmospheric and topographic effects in the data.

Fast line-of-sight atmospheric analysis of spectral hypercubes was developed by Adler-Golden et al.[37] It retrieves the land surface reflectance without using ground measurements. Staenz et al.[38] developed imaging spectrometer data analysis system to process hyperspectral data by removing sensor and calibration artifacts. It converts at sensor radiance to surface reflectance and analyses the hyperspectral data. Qu et al.[39] developed high-accuracy atmospheric correction for hyperspectral data. This model corrects the water vapor and other gases (such as CO_2 and methane).

4.2 *Dimensionality Processing*

Once corrected, the hyperspectral data still have redundant spectral information, which need to be processed. To reduce the computational costs and processing time without losing the useful information, the data should be dimensionally diminished. Dimension reduction techniques can be categorized into different groups such as unsupervised and supervised, linear and non-linear approaches. Principal component analysis (PCA), minimum noise fraction (MNF), and independent component analysis (ICA) are the most popular unsupervised dimension reduction approaches. PCA is a linear widely used technique that searches to magnify the variance within the new and lower subspace.[40] MNF is a well-known denoising technique that transforms noisy original hyperspectral data cube to channel images with the increasing noise level.[41] ICA is a statistical mechanism that transforms the data into maximally independent and non-Gaussian subparts.[42,43] This method uses virtual dimensionality to determine the number of independent components, which should be retained.[25] Supervised methods are performed to extract more useful information using the prior knowledge of training samples. Commonly used supervised dimension reduction algorithms include Fisher's linear discriminant analysis[44] and discriminative locality alignment (DLA).[45] Local Fisher's discriminant analysis[46] and semisupervised DLA[45] are some variants of those techniques.

In order to overcome some problems that arose from traditional dimension reduction methods, sparsity-based techniques such as sparse-graph-based discriminant analysis[47] and multiple-features-combining[48] method were developed to enhance the dimension reduction results. The incorporates the spectral, texture apart from traditional methods; new methods based on machine learning communities have been developed for processing hyperspectral images. A number of metric learning algorithms such as relevant component analysis,[49] neighborhood component analysis,[50] information-theoretic metric learning,[51] and ensemble discriminative local metric learning[52] solve the problems in hyperspectral analysis. In addition, different manifold learning-based dimension reduction methods are proposed to display the non-linear structure in hyperspectral images including locally linear embedding,[53] Laplacian eigenmap,[54] isometric mapping,[55] neighborhood preserving embedding (NPE).[56] Hypergraph learning methods have also been introduced to explore the multiple adjacency relationship in hyperspectral data and discover the complex geometric structure between hyperspectral images.[57] Discriminant hyper-Laplacian projection,[57] semisupervise hypergraph embedding,[58] local pixel NPE,[59] and spatial–spectral regularized sparse hypergraph embedding[57] are some types of graph embedding methods for dimensionality reduction of hyperspectral images.

4.3 *Endmember Extraction Methods*

Due to enhanced spectral resolution of HSI, extraction of hyperspectral endmember is a fundamental step in the hyperspectral data processing. An endmember is a pure and diagnostic

signature that can be used to specify a spectral class. It should be noticed that each endmember does not need to be a pure pixel.[60] There are several endmember extraction algorithms that are broadly grouped into two main classes including convex geometric-based and statistical-based categories.[12] In widely used linear unmixing model, the spectra of each pixel vector are regarded to be a linear combination of endmembers weighted by their corresponding abundances.[61,62] There are two main groups of endmember extraction methods within the linear spectral unmixing algorithms as pure-pixel and non-pure-pixel methods. In these methods, the hyperspectral data are considered as simplex, and its endmembers are constituting its vertices. The pure-pixel approach assumes that there is at least one endmember in the image scene and applies simplex growing algorithms or maximum volume transform to find the endmembers within the hyperspectral data cloud.[63,64] The popular algorithms involve pixel purity index (PPI), and N-finder algorithm (N-FINDR), vertex component analysis, automatic target generation process, and convex cone analysis are typical pure-pixel or simplex growing methods.[47,48] In order to overcome the issues in pure-pixel endmember extraction, non-pure methods have been developed that use the shrinking simplex algorithms or minimum volume transform techniques.[64] Optical real-time adaptive spectral identification system (ORASIS), minimum volume constrained non-negative matrix factorization (MVC-NMF), minimum volume enclosing simplex (MVES), minimum volume simplex analysis (MVSA), and abundance separation and smoothness constrained non-negative matrix factorization are developed as non-pure-pixel extraction algorithms.[64] The ORASIS as the linear mixture model, developed by the Naval Research Laboratory, consists of series of stepwise algorithms including prescreener, basis selection, and endmember selection to unmix each pixel of dataset to different endmembers.[65,66] This method considers all the data pixel inside a simplex with endmember vertices. According to Chang,[66] the functionality of this method declined in hyperspectral data with low signal-to-noise ratio (SNR). MVC-NMF has been developed by Miao and Qi[67] as a non-pure pixel-based algorithm, which is convex geometry-based algorithm. This method tries to fit simplex while its volume is minimal and encompass the data cloud.[67] Nouri et al.[68] used particle swarm optimization to improve MVC-NMF method for mineralogical unmixing of hyperspectral data with high SNR.[68] MVSA is another linear mixture model for endmember extraction that was developed by Li and Bioucas-Dias.[69] This algorithm tries to fit a minimum volume simplex to the hyperspectral data, which contains the abundance fractions to belong to the probability simplex.[70] In this method, it is assumed that pure pixel may not exist in the hyperspectral data, which can address a common situation in hyperspectral data with highly mixed pixels.[70] Motivated by Craig's belief, Chan et al.[71] developed linear-based model called MVES algorithm in which vertices of the simplex enclose all the observed pixels. In this method, the simplex should estimate all the endmember signatures with high fidelity.[72] Non-linear geometrical unmixing methods have been used less than linear techniques. Broadwater[73] introduced non-linear kernel methods to solve the unmixing problem in high-dimensional hyperspectral data. Heylen[74] introduced geodesic simplex volume maximation methods under non-linear mixing assumptions to extract hyperspectral endmembers. The statistical-based endmember extraction methods use statistical representations.[63] Based on parametric, non-parametric, and spatial statistic representations, different statistical-based unmixing methods have been developed. Stochastic mixing model, which assumes Gaussian distribution for each endmember, is an example of statistic-based algorithms that used parametric representations.[75] ICA is proposed by non-parametric statistical unmixing approaches. ICA-based abundance quantification algorithm and combination of ICA and independent factor analysis are some kinds of non-parametric statistical endmember extraction approach.[63] Automated morphological endmember extraction, iterative error analysis, and spatial–spectral endmember extraction (SSEE) are statistical unmixing methods that used spatial statistics to improve the endmember selection.[12,63]

5 Image Classification Techniques

Image classification generally refers to a set of techniques to assign different classes to all the pixels in the digital image. Since the advent of hyperspectral remote sensing, different hyperspectral image classification approaches and algorithms have been developed and evolved.

Due to high dimensionality, mixed pixels, and a smaller number of training samples, image classification procedure for high-spectral-resolution hyperspectral images is facing more challenges. However, various methods have been designed and employed to overcome these challenges. The image classification mainly categorized into three main groups including supervised, unsupervised, and semisupervised techniques. Over the last decades, based on various criteria, supervised and unsupervised image classification has been categorized into further groups including per-pixel and subpixel, parametric and non-parametric, soft and hard, spectral and spectral–spatial, and per-field.[25,76,77]

In supervised classification, the image analyst uses training samples (known) obtained from expert knowledge to specify different spectral signatures or pixel values of the image as to different classes.[25] Based on prior knowledge, the user selects sample representative pixels of a known cover type or pattern in an image as the specific class and assign it as training sites. Then these training sites will be used as references for the classification of other pixels in the image. Some of the important supervised classifiers include maximum likelihood classifier (MLC), support vector machine (SVM), spectral angle mapper (SAM), decision tree, and artificial neural network (ANN).[25]

In unsupervised classification techniques, there is no need for the analyst's extensive prior information and contribution. Helping to find different clusters in data, this approach can be utilized for feature extraction and segmentation. In this method, the classes are created purely based on spectral information not manual visual interpretation. *K*-means, iterative self-organizing method (ISODATA), and clustering are some of the common unsupervised classifiers.[78]

Semisupervised classification utilizes some available known reference information along with undefined data. Semisupervised random was forest recently used for hyperspectral image classification.[79]

Parametric classification techniques consider data to have a normal distribution pattern and deal with statistical parameters such as mean vector and covariance matrix. In the case of complex landscape, the classification results should be noisy. In addition, insufficient, nonrepresentative, and multimode-distributed training samples result some ambiguities in image classification. Combining spectral data with ancillary information and non-statistical data in parametric approach make some difficulties for remote sensing image classification.[77] However, due to its robustness and easy implementation, the MLC is one of the most widely used parametric classification.

In non-parametric classifier, no statistical parameters of the distribution of the input data are required. It is facilitated in this approach to integrate non-remote sensing data in the image classification procedure. Decision tree classifier, expert systems, SVM, deep learning, and neural network become typical examples of non-parametric classifiers widely deployed in remote sensing image classification.[25]

Per-pixel classifier creates and assigns a signature through combing the spectra of the feature set from the entire pixel to a single class. Not considering the mixed pixel problem, the resultant signature includes the integration of all the materials available in the training set of pixel.[25,77] Most of the classifiers such as MLC, Euclidian distance, ANN, decision tree, and SVM, SAM, binary encoding, and spectral feature fitting are important per-pixel classifiers. Due to poor spatial resolution of hyperspectral remote sensing images, each pixel spectrally is not pure and normally contains a mixture of two or more target materials.

Subpixel classifiers have been introduced to overcome the challenge of existing different materials in a pixel. These techniques consider the spectral value of each pixel as the integration result of linear or non-linear combination of pure materials. These techniques assign the exact class for each pixel for the classification of the medium- to low-spatial-hyperspectral remote sensing images. It employed different linear and non-linear unmixing models for subpixel level spectral matching.[25,76]

Linear unmixing models consider each pixel as a linear combination of a set of spectral fingerprints as endmembers respect to their abundances. In other words, in linear unmixing models, the subpixel component can be physically distinct in their reflectance property. In geological applications, the different mineral fields or library spectra have been applied for mineral identification and their abundance. The most popular model for spectral unmixing is linear mixing

model (LMM). Some endmembers or pure pixel detection algorithms such as N-FINDR and PPI are performed in this model.

Non-LMMs consider that the light photon has been affected by different earth surface materials before detection by the sensor. Various types of photon interaction in the mixed pixel in non-LMM are vertical mixing (tree canopies) and horizontal mixing (granular mixtures) and both. Bilinear models, intimate mixture models, neural-network-based models, kernel-based models, physical modeling, and manifold techniques are the non-LMMs have been used by many researchers.[77,80]

Spectral classifiers consider hyperspectral images as only spectral data without any concerns about spatial information. Due to high level of mixing in the spatial distribution of the different classes, spectral classifiers produce noisy results.[25] Although the spectral classifiers have the conceptual simplicity and computational effectiveness, they are not able to effectively separate a number of land cover materials. MLC and ANN are some of the important spectral classifiers.

Spatial-contextual approaches were developed to get higher accuracy classification.[25] In these techniques, spatial information from adjacent pixels are extracted to get a better classification result. Some smoothing techniques including fuzzy logic and neural network can be performed before the main classification approach. Texture extraction, MRFs modeling, image segmentation, and object-based image analysis are the main spatial-contextual remote sensing methods. Spectral–spatial classifiers are mostly considered for hyperspectral image processing. In these approaches, parametric and non-parametric classifiers are performed before the employment of the spatial classifiers.[76,81]

Soft classifiers employ conditional probability to make a decision boundary for classification of target in the image.[77] In this method, each pixel can belong to more than one class and there is a gradient between each class. Linear mixture modeling and Fuzzy classification are the most common soft classification technique.

Hard classifiers in contrast make the decision boundary of the target without doing the probability assessment. They consider each pixel belonging to the class it most closely resembles. The results of this classification have lower accuracy than soft classification approaches. ISODATA, parallelepiped, *K*-means, maximum likelihood, and neural networks are the most important hard classifiers.[76]

Considering single or multiple classifier(s) are another criterion to group image classifiers.[25] Single classifier assumes a class label to a given pixel. One of the most well-known classifiers that have been used as a single classifier is SVM. It creates linear decision boundaries to classify multiple classes. This method defines different training samples by finding maximum margin hyper planes in the space of the mapping sample.

In ensemble or multiple classifiers, a set of different classifiers are performed to assign a class label for a given pixel. It could increase the accuracy of the classification result. In this approach, it should be considered that combination of the classifiers has benefit to increase the accuracy without any drawbacks.[78,81]

Prior reference data requirement also establishes a distinct category to group spectral image classifiers. In the case of no prior reference data, the direct spectral patterns of a pixel are used to image processing. In contrast, some techniques utilize the predefined representative information as reference data for image processing procedure.[11] These methods are categorized as knowledge-based and data-driven approaches.

Knowledge-based techniques incorporate knowledge from spectral features of the different materials. These approaches apply distinct characteristics of absorption features such as position, depth, asymmetry, and width in different materials.[11,14,19,82,83] Band calculation, feature mapping, expert system, spectral deconvolution, wavelet analysis, and scattering theory constitute different methods constituting knowledge-based techniques.

Data-driven methods require the hyperspectral data and additional reference data (spectra).[66,84] The reference data are commonly assigned as training classes or endmember sets, which are imported from a spectral library or derived from the image. Different classifications included in the per-pixel and subpixel classifiers are categorized in data-driven classifiers.

6 Geological Applications

6.1 *Lithological Mapping*

High-spectral-resolution properties of the hyperspectral remote sensing make it as an important potential to accurately recognize and map the earth surface materials.[29,33] Hundreds of contiguous spectral bands of hyperspectral images can be used to extract pixel spectrum for mineral and rock discrimination.[33] Performing mineral and lithological mapping from hyperspectral images is generally due to comparison of unknown spectrum to a reference spectrum.[82] Spectral absorption characteristics of different minerals are mostly related to vibrations of Fe^{2+}, Fe^{3+}, Al-OH, Mg-OH, OH-, and CO_3 in the VNIR and SWIR. Minerals with Fe^{2+} and Fe^{3+} have an absorption peak at 1.03 and 0.64 μm, respectively. Al-OH-bearing minerals have a significant absorption peak at 2.15 to 2.22 μm, whereas the most important absorption peak position of Mg-OH minerals occur at 2.30 to 2.39 μm. CO_3 group minerals show a distinct absorption peak at 2.35 μm.[14,16,18–20] VNIR-SWIR region is mostly used for alteration minerals mapping including Fe-OH, Mg-OH, Al-OH, and CO_3-bearing minerals. However, these spectral features can be applicable for the Mg, Fe, and Al silicate minerals such as olivine, pyroxene, mica, and amphibole. Mineral spectral features of silicate minerals mostly attributed to vibration of Si–O bonds in TIR region.[14,16,19]

Kumar et al.[85] proposed an automated lithological mapping approach on AVIRIS-NG hyperspectral data from gold-bearing granite-greenstone belt of the Hutti area (India). In that approach, they employed spectral enhancement techniques such as PCA and ICA and different machine learning algorithms (MLAs) to get an accurate lithologic map (Fig. 4). However, they utilized conventional geological map and spectral enhancement products derived from ASTER data to generate a high-resolution reference lithology map. Among different MLAs, they found SVM using joint mutual information maximization (JMIM)-based optimum bands to have a better performance with higher accuracy.

Salehi et al.[86] investigated the performance of HyMAP hyperspectral images and Sentinel-2, ASTER and Landsat-8 OLI spaceborne multispectral data for lithological mapping of mafic–ultramafic rocks in lichen-covered area in south west of Greenland. They performed EnMAP geological mapper (EnGeoMAP) and iterative spectral mixture analysis (ISMA) algorithms. They used structural similarity index measure to compare the output of classification results of airborne data with available geological map and spaceborne data with reference HyMAP data. According to their results, the HyMAP and spaceborne multispectral data can provide geological maps comparable to geologic maps over the less accessible arctic regions. Three different ultramafic rocks (dunite, peridotite, and pyroxenite) and one mafic rock (gabbro) has been mapped based on VNIR and SWIR spectral analyzing.[86] They found EnGeoMAP algorithm to have a better performance for dunitic rocks and ISMA method for peridotite and pyroxenite units.

Harris et al.[87] performed several methods on airborne PROBE hyperspectral data from the test site in southern Baffin Island, Canada to produce lithological–compositional map. After masking out and eliminating water bodies, ice, snow, and vegetation areas from analysis, they applied MNF transformation to reduce the large dataset to a fewer number of components that have the main information. They performed matched filtering (MF) to extract the user defined endmembers due a partial unmixing method. The end members were selected by color discrimination in MNF composite images. They discriminated one lithological group (metatonalites) and three compositional units (psammite, quartzite, and monzogranites).

Zhang and Li[88] implemented an evolved SAM approach using EO-1 Hyperion hyperspectral images in lithological mapping in two different arid areas in China. They employed two different methods to improve the lithological mapping performance. In the first method, they used the mean of spectral derivatives and mean of original spectral data in SAM to improve class separability. In the second approach, multiple reference spectra were utilized to accommodate the spectral variability. As the result, they mapped Carboniferous-Permian volcanic-sedimentary rocks, Jurassic sedimentary rocks, granite, and quaternary sediments in Junggar area and Cambrian, Ordovician, Silurian, Devonian sedimentary rocks including dolomite, shale, marl, siltstone, quartzose sandstone, and sandstone, and quaternary sediments in Kalpin area.

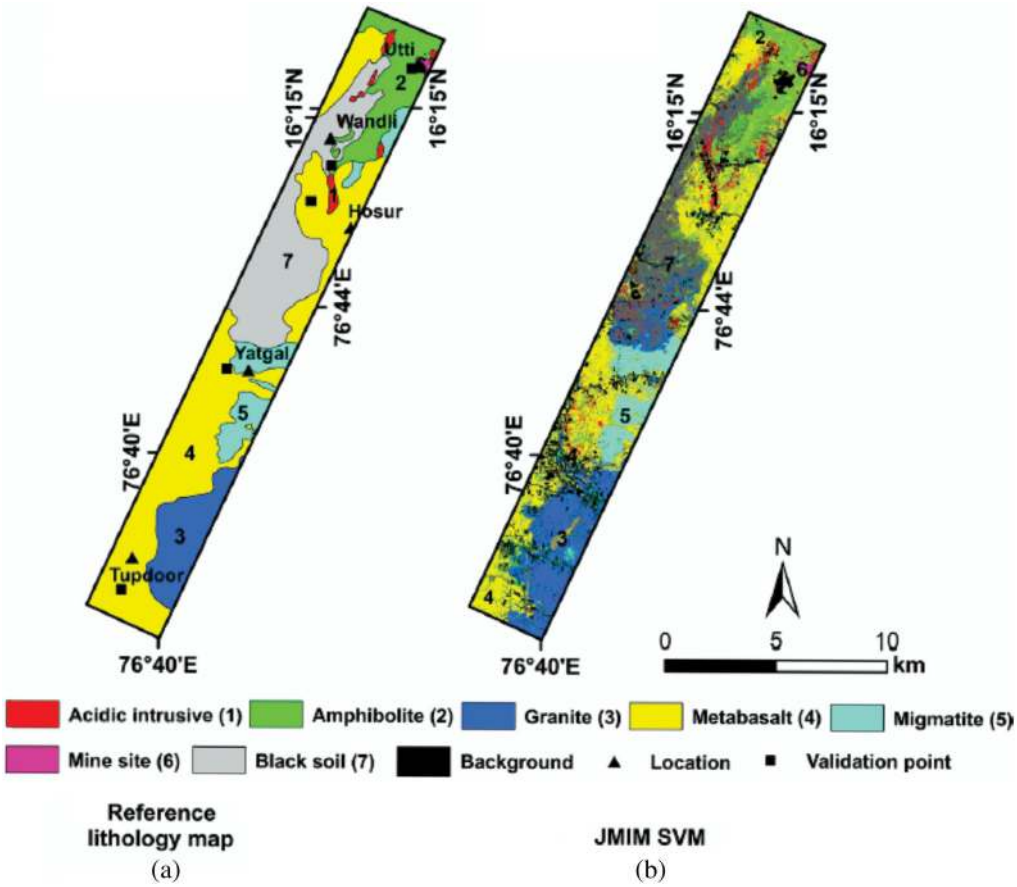

Fig. 4 (a) Reference lithology map derived from spectral enhancement products using ASTER and (b) lithological classification map generated from SVM using JMIM-based optimum bands of AVIRIS-NG hyperspectral data from gold-bearing granite-greenstone belt of the Hutti area (India).[85]

Dadon et al.[89] used EO-1 Hyperion hyperspectral data for stratigraphic and lithologic mapping. They performed SAM supervised classification after some preprocessing and endmember extraction processes. They separated different plutonic (monzogranite, granite, and granodiorite), volcanic (green tuffs and basaltic lava), and sedimentary (limestone, sandstone, conglomerate, and dolomite shale) rocks form the Dana Geology National Park (south-west Jordan) after stratigraphic and lithologic mapping process.

Pal et al.[77] considered the VNIR and SWIR bands of Hyperion spaceborne hyperspectral data and ASTER and Landsat 8 multispectral images. They implemented four-step technique for lithological mapping of Udaipur area, Rajasthan, western India. They employed a hybrid classification method involving minimum distance, SAM, spectral information divergence, and SVM to optimize lithological mapping. Pal et al.[77] used this method to discriminate different sedimentary and metamorphic lithoclasses including quartzite, phyllite, graywacke, dolomite, mafic-metavolcanics, migmatite, graphitic metapelites, and quartzite-arkose-conglomerate in the Udaipur area.

6.2 *Mineral Mapping and Mineral Exploration*

Mineral mapping and determination of surface composition for mineral exploration purposes is one of the most important applications of hyperspectral remote sensing. There are different ore deposits classifications based on different fundamental genetic processes: magmatic, hydrothermal (magmatic), sedimentary, metamorphic, and mechanical process. Different mineralization systems are dominantly associated with different alteration associations and mapping surface mineralogy can be considered as vectors to ore deposits.[90] A schematic overview of

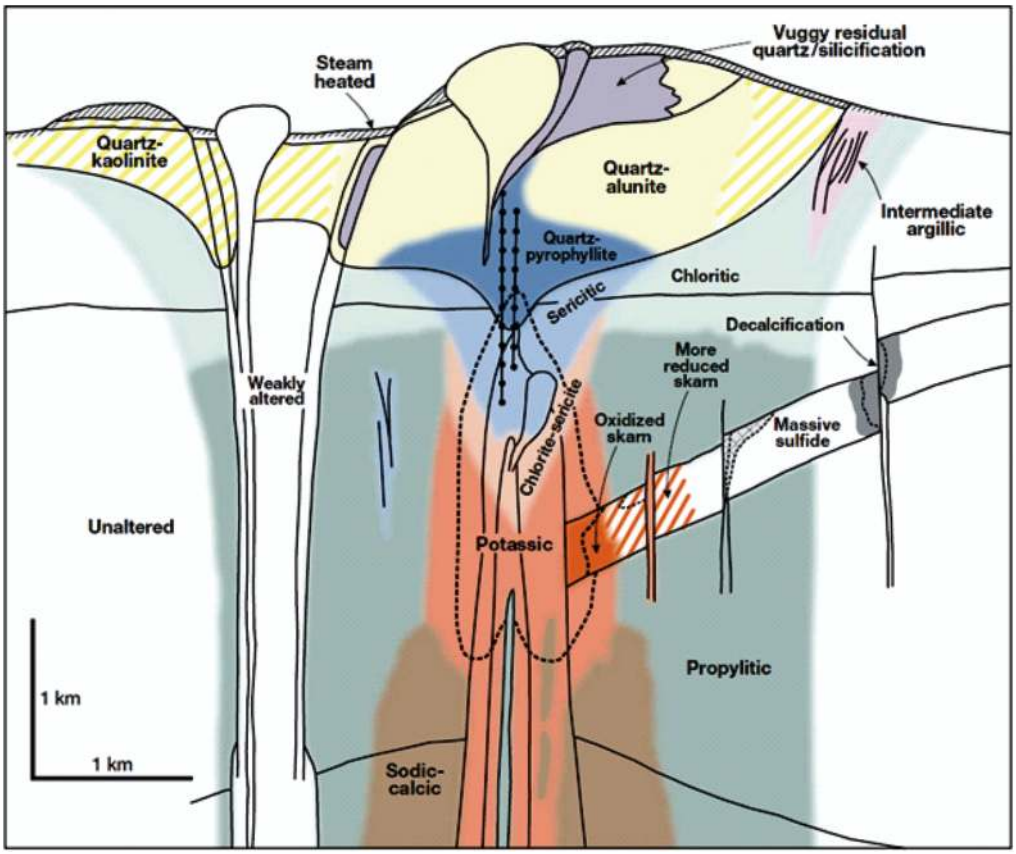

Fig. 5 Generalized alteration-mineralization zoning pattern for PCDs.[91]

intrusion-related mineral deposits and associated alteration patterns have been shown in Fig. 5.[91] Figure 6 shows some diagnostic different alteration assemblages along with some of the main ore deposits. Most of the alteration minerals have distinct spectral features in VNIR-SWIR and TIR region.[92]

Magmatic hydrothermal deposits include several important ore deposit types such as porphyry, epithermal, skarns, intrusion-related, volcanogenic massive sulfide (VMS), iron oxide copper gold (IOCG) uranium rare earth element (REE), alkaline complexes, and spreading centers sea-floor smokers.[93] Hydrothermal intrusion-related ore deposits directly formed within or with a distance with igneous intrusions. There are spatial alteration patterns and mineral assemblages in these deposits. However, they have some genetic relationship with the fractures and faults in the host rocks. They include alteration patterns such as feldspathic, sericitic, silicic, greisen, calc-silicate, and/or advanced argillic assemblages.

Jintanzi gold province (China) is one of the intrusion-related gold deposits. This deposit is mostly related to quartz veins within the granites and associated with different order faults. Using spaceborne Tiangong-1 HSI and airborne short-wave infrared airborne spectrographic imager (SASI) data, Liu et al.[94] tried to produce alteration mineral maps via SAM algorithm. They considered JPL and endmembers extracted by SSEE as the reference spectra. Using either set of the reference spectra, they detected alteration muscovite, kaolinite, chlorite, epidote, calcite, and dolomite as the hydrothermal minerals. Figure 7 shows the mineral maps derived from image endmembers from SASI and Tiangong-1 hyperspectral data. According to their results and previous studies, the distribution of the alteration minerals has been distinctly controlled by the gold-bearing quartz veins and faults.

Epithermal Au–Ag deposits have been considered as important gold and silver sources in the world, which commonly distributes along the convergent plate margins.[95] Extensive geological studies have been done on different epithermal gold-silver deposits. However, several researchers have considered the application of remote sensing data in order to investigate and model the

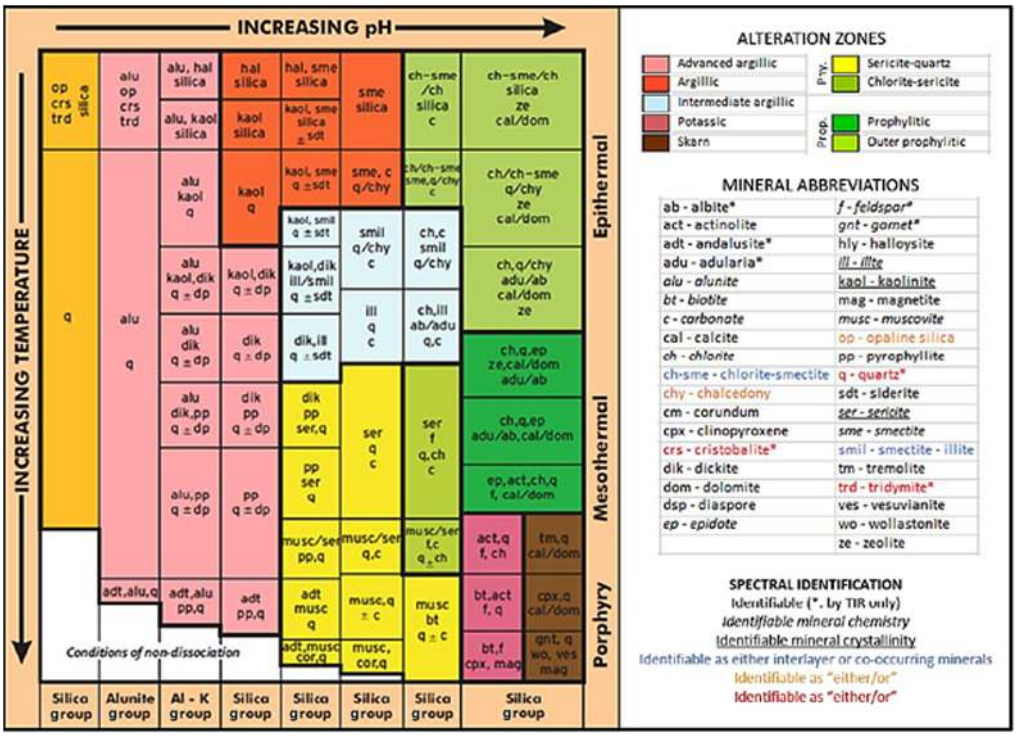

Fig. 6 Common alteration minerals in different ore deposits.[92]

hydrothermal alteration mineral mapping in these deposits.[96–99] Silisic, potassic, argillic, propylitic, and zeolitic are the most common hydrothermal alteration minerals in epithermal deposits. Rodalquitar deposit (southern Spain) is one of the most popular epithermal gold and silver deposits that have been extensively studied in geochemical aspect to understand the mineralization process. Also numerous geological remote sensing studies have been conducted to generate mineralogic map of the area. van der Meer et al.[97] performed wavelength mapper and QuanTools to derive absorption feature from HyMAP hyperspectral images of Rodalquiar epithermal deposit. They used absorption feature position as a key to find the mineral chemistry variations such as Al–Mg versus OH, which can be interpreted in terms of fluid compositions and temperature. Figure 8 displays the alteration mineral maps of Rodalquiar epithermal system constructed via Quantools and wavelength mapper.[97]

PCDs constitute the largest source of copper and a major source of molybdenum, gold, and silver in the world.[100] These deposits commonly have diagnostic broad alteration patterns with distinctive minerals. Typical alteration types in PCDs include potassic alteration in the core, which is surrounded by sericitic, argillic, and propylitic zones.[91] Subtle variations in the alteration minerals could be considered as the high economic potential in PCDs. For example, zonation of chemical variation of white mica in phyllite alteration is a proxy of chemistry of ore forming fluid.[16,101] Figure 9 shows the variation of white mica chemistry, which has different SWIR wavelength characteristics in typical cross section of PCD.[16] Although several spaceborne and airborne hyperspectral data have been used for porphyry Cu exploration, there are a few literatures that investigated them.[102–104] Sarcheshmeh PCD (southern Iran) located in the Orumieh-Dokhtar magmatic arc is one of the best sites for studying alteration related to PCD. Using Hyperion data, Zadeh et al.[104] (2014) identified characteristic alteration minerals including biotite, muscovite, illite, kaolinite, goethite, hematite, jarosite, pyrophyllite, and chlorite via subpixel mixture tuned matched filtering (MTMF) method (Fig. 10). Discriminating minerals such as biotite and iron oxide is one of the most important evidence for PCD exploration. Bishop et al.[102] used SAM and MTMF techniques to discriminate and map the alteration mineral assemblages from Hyperion data in the Pulang, PCD (Yunnan, China). They determined argillic alteration, iron-oxide-, and sulphate-bearing minerals in the target deposit.

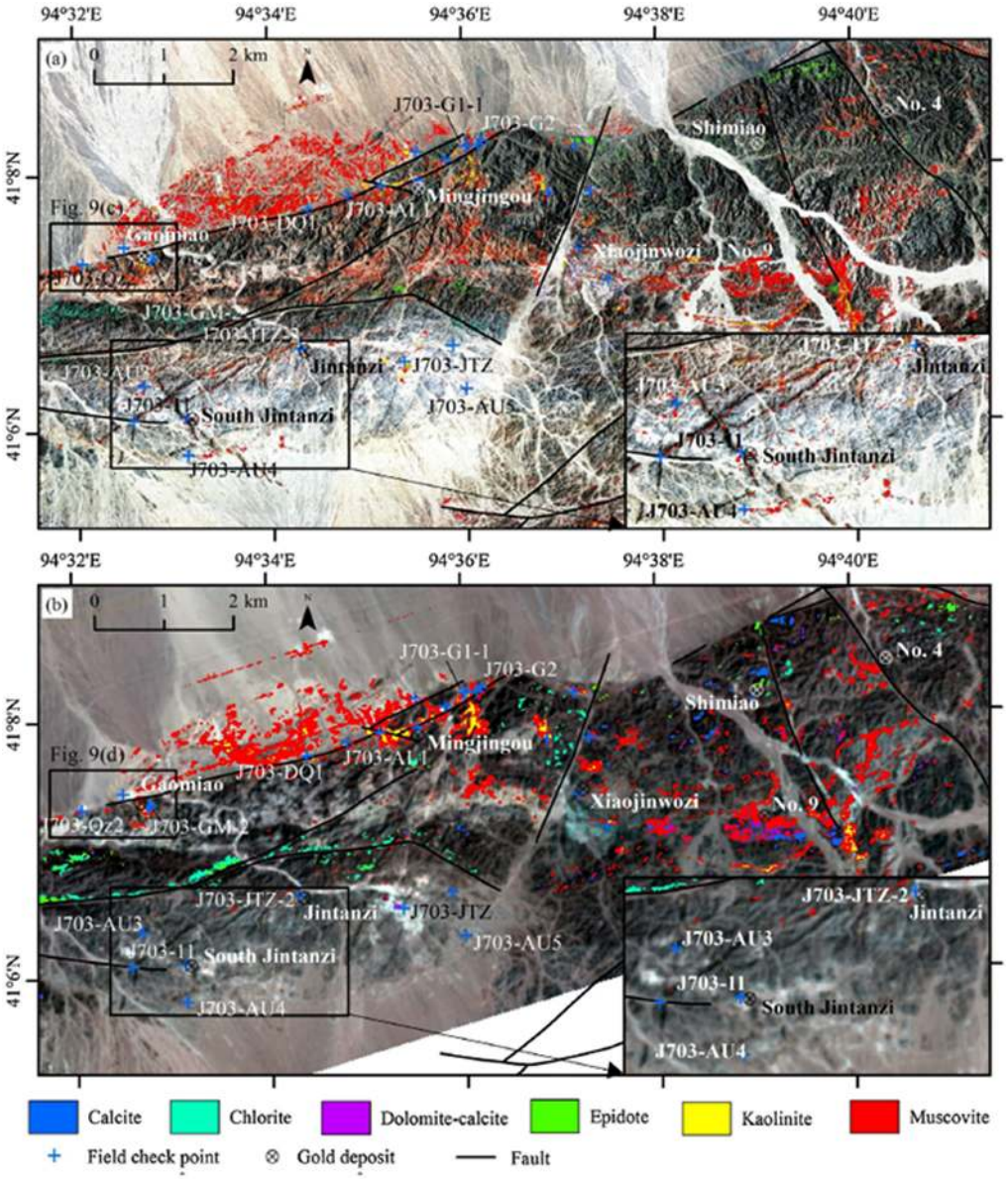

Fig. 7 Mineral maps derived from the use of image endmembers applied to (a) SASI data and (b) Tiangong-1 HSI data from Jintanzi gold province (China).[94]

IOCG (± U-REE) deposits are a group of magmatic-hydrothermal deposits, which are structurally controlled and commonly associated with different alteration zones. The alteration zones of host rocks begin with sodic alteration, which changed to sodic-calcic and potassic toward the main Fe-oxide mineralization.[105] Deposits with more developed potassic alteration commonly have intensive magnetite mineralization. Surficial rocks often show sericitic and silisic alteration. Investigation of Corriveau et al.[106] show that each alteration type in this deposit type has a unique spectral signature. Potassic and sodic alterations are mostly distinguished by the location of hydroxyl feature (OH-) near 2.200 μm. According to their results, airborne or spaceborne hyperspectral data have a potential capability to map exposed alteration maps around the IOCG deposits. Tappert et al.[107] used the infrared reflectance spectra to discriminate the high-Al and low-Al phengite as a potassic mineral identified at the Olympic Dam IOCG deposit (south Australia). The phengite minerals in the heavily sericitized ore-bearing rocks have lower Si content, higher Al content, and lower Mg content that the phengites formed in the weakly sericitized altered host rocks. High-Al phengite has a spectral absorption feature at 2.206 μm, whereas low-Al type is recognized by the absorption feature at 2.213 μm. Therefore, spectral absorption feature can be

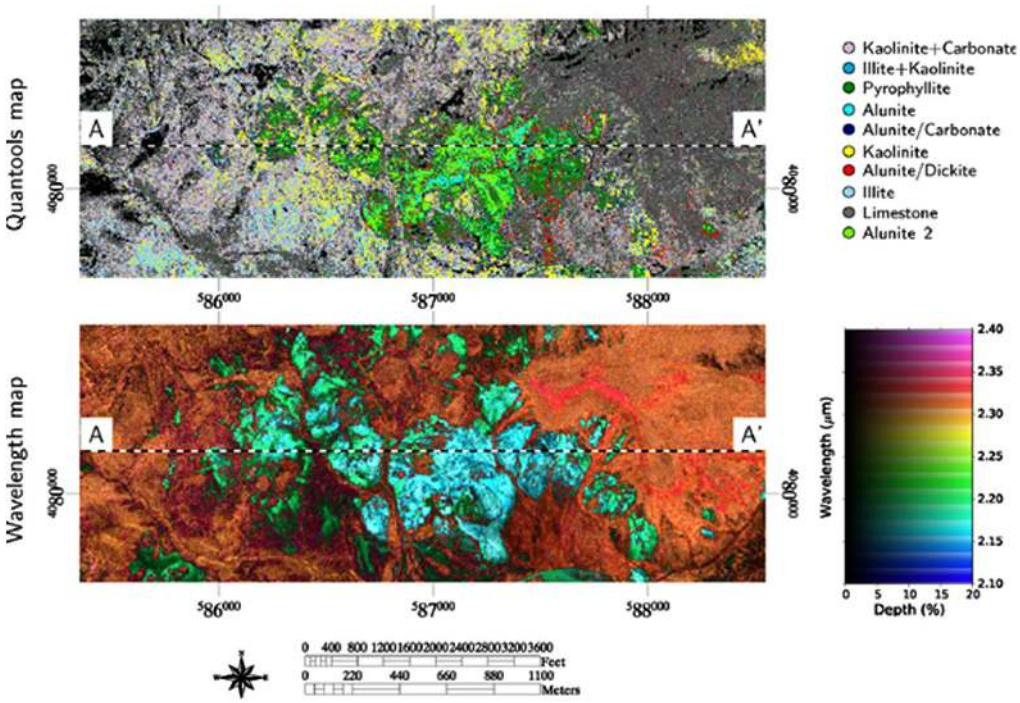

Fig. 8 From top, mineral map constructed with Quantools and mineral map constructed with the wavelength mapper using HyMAP data of Rodalquilar epithermal system (southern Spanish Gabo de Gata volcanic area).[97]

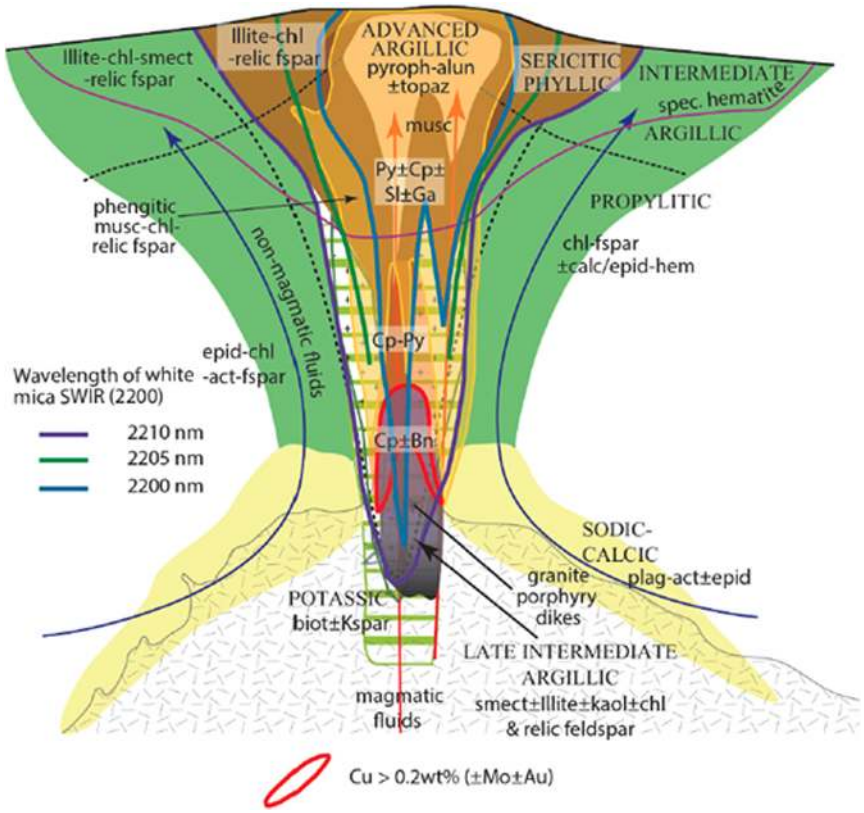

Fig. 9 Typical cross section of PCD, showing generalized Al(OH) 2.200 μm absorption of different white mica in phyllic alteration.[16,101]

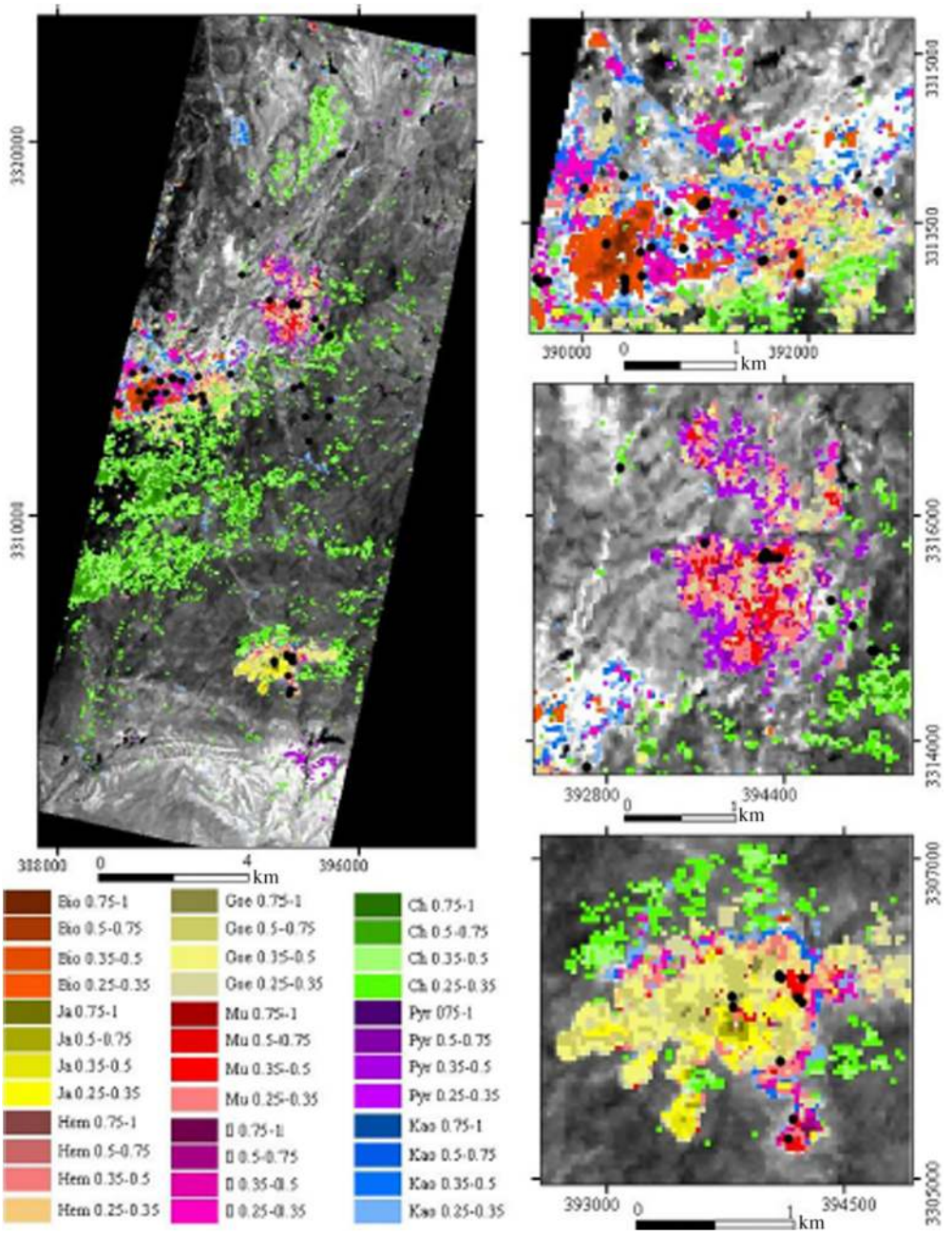

Fig. 10 Final classification image map of alteration minerals at Sarcheshmeh deposit (southern Iran) derived from MTMF algorithm. Bio, Mu, Il, Kao, Goe, Hem, Ja, Pyr, and Ch indicate biotite, muscovite, illite, kaolinite, goethite, hematite, jarosite, pyrophyllite, and chlorite, respectively.[104]

representative of the sericitic alteration degree due hydrothermal alteration related ore forming process. Laukamp et al.[108] used HyMap airborne hyperspectral data to derive high-resolution alteration mineral map of Mount Isa Inlier IOCG deposit (Australia). They employed hyperspectral data as a tool for hydrothermal alteration detection and fluid pathway identification related to Cu–Au IOCG deposits.

VMS deposits are kind of metal sulfide deposit, mostly copper and zinc, which formed near the sea floor. Similar to other magmatic hydrothermal ore deposits, they have alteration patterns, which have been formed via circulation of ore forming fluid through the host rocks.[109] The hydrothermal alteration patterns include potassic, advanced argillic, argillic, sericitic, chloritic, and carbonate propylitic from the inner mineralized core to the peripheral area.[110]

There are different hyperspectral remote sensing studies on the several important worldwide VMS deposits to characterize the hydrothermal systems. van Ruitenbeek et al.[111] used HyMAP hyperspectral data to evaluate white mica distribution pattern around Panorama VMS deposit (western Australia). They used the advantages of different absorption features at 2.185 to 2.235 μm of Al-rich and Al-depleted white mica to map the alteration patterns and alteration related fluid. Using AVIRIS-NG hyperspectral data, Samani et al.[112] discriminated alteration minerals including calcite, muscovite, and chlorite in the Ambaji-Deri area (northwestern India). They performed different image processing approaches such as MNF, PPI, *N*-dimensional visualization, and SAM classification. They matched the endmember spectra with the USGS spectral library. Figure 11 shows the observed spatial distribution of different hydrothermal minerals in the Ambaji-Deri region. Laakso et al.[113] used different scale hyperspectral data such airborne, laboratory, and field methods for VMS mineral exploration in Canadian Arctic. They took the advantages of the spectral Al-OH and Fe-OH absorption features in the SWIR wavelength region of biotite and chlorite, which reflect the chemical compositional changes with the distance to the mineral deposit. Fe-OH has an absorption feature at 2.254 μm in proximal areas to the ore deposit while it changes to 2.251 μm in the distal areas. In addition, proximal areas have the Al-OH absorption feature at 2.203 μm in contrast with the absorption feature at 2.201 μm in distal areas.

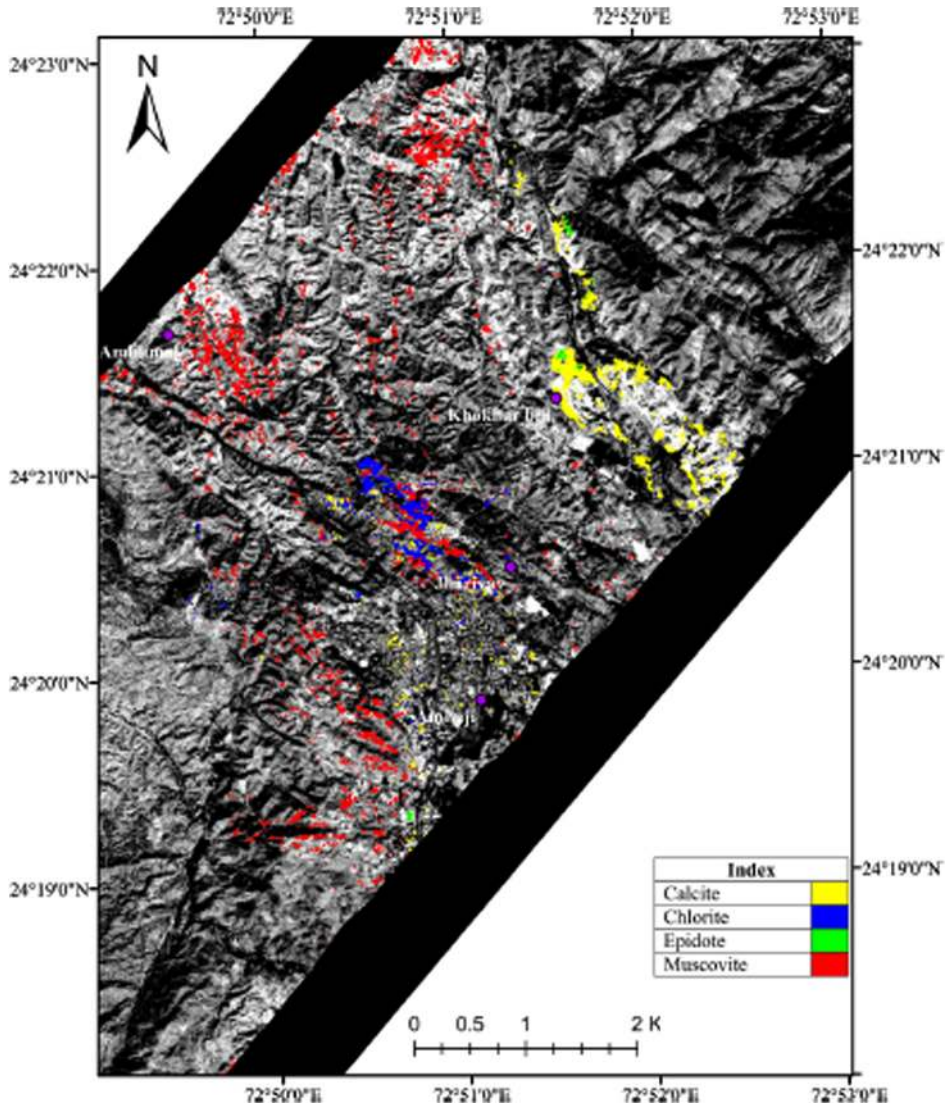

Fig. 11 Spatial distribution of the carbonate minerals at northeast of Khokhar Bili and alteration minerals around Jharivav and Amblimal.[112]

Skarn deposit is another type of magmatic hydrothermal deposits, which have been formed due to metamorphism and hydrothermal alteration of carbonate-bearing rocks. They are considered as the potential source of different ore minerals such as copper, tungsten, iron, molybdenum, zinc, and gold. There is a zonation pattern in skarn deposits from garnet in the proximal to pyroxene in distal areas and pyroxenoid such as wollastonite in the skarn and marble contact.[114] However, individual skarns may show systematic compositional changes in these zonation pattern. Thus detail mineralogy of skarns and their zonation can be useful in ore exploration processes.

There are several hyperspectral remote sensing studies to detect alteration zones around skarn deposits as a proxy to skarn type ore deposit exploration. Xu et al.[115] used spaceborne Hyperion and close-range field hyperspectral data from Dapingliang skarn copper deposit (China) to identify the mineral zones around the skarn deposit. They distinguished pixels related to skarn using SAM from spectra overall shape and absorption bands spectral shape. Field data were applied to directly identify alteration mineral instead of just surface materials, which probably do not have any direct relationship with the ore mineralization. Tian et al.[116] used the SWIR spectral analyses to detect alteration minerals including sericite group minerals (montmorillonite, illite, and muscovite), kaolinite, and carbonate minerals (calcite, ankerite, and dolomite), with minor chlorite, halloysite, and dickite around Jiguanzui Cu-Au (Eastern China) deposits. According to their results, Fe-OH absorption feature of chlorite (2.241 to 2.263 μm) becomes shorter to the distal areas. Also minimum Al-OH absorption feature of 2.209 μm can be a useful vectoring tool to the ore deposit.

6.3 *Environmental Geology*

Environmental geology is one of the geological applications to solve environmental problems derived from interaction of human with geologic environments like mineral resources. For instance, the mining projects and abandoned mines are one of the main agents contributing to cause serious ecological pollution. Vegetation, soil, water resources, and human can be threatened by wastes that were left over including lead, zinc, cadmium, and some toxic minerals.[117,118] These wastes with a widespread distribution have the high potential of pollution. As mentioned in the foregoing sections, hyperspectral remote sensing has a powerful potential to detect earth surface materials such as different minerals and elements. Therefore, it can be used to characterize and monitor the mineralogy of mine waste surfaces to predict the potential source of pollution including metal leaching and acidity. Since the application of hyperspectral remote sensing in geology, different studies have been done to monitor pollution from various mining areas.[117,119–125]

One of the processes that have been caused pollution in the mining area is pyrite oxidation.[123,125] This process may produce acidic water, which has gradually crystallized different Fe-bearing secondary minerals in the way from the mining waste. These minerals include copiapite,[61] jarosite $[(K, H_3O, Na)Fe_3(SO_4)_2(OH)_6]$, schwertmannite $[Fe_8O_8(OH)_6SO_4]$, ferrihydrite $[Fe_5HO_8, 4H_2O]$, goethite $[\alpha\text{-}FeO(OH)]$, and hematite $[\alpha\text{-}Fe_2O_3]$.[123] These secondary minerals are spectrally identifiable due to their diagnostic spectral reflectance signatures. Swayze et al.[123] used AVIRIS spectral data to evaluate mine waste in the California Gulch Superfund Site. They used 0.4 to 2.5 μm spectral range of hyperspectral data to detect secondary Fe-bearing minerals and create a mineral map to highlight the areas, which have the potential for acidic drainage and predict the leaching and acid generation sites at Leadville mining district (Fig. 12). They performed Tetracorder algorithm to produce the Fe-bearing minerals map. Davies and Calvin[126] have used airborne hyperspectral data to characterize acidic mine waste at the Leviathan mine Superfund site in the eastern Sierra Nevada. They used SAM and MF algorithms to map minerals related to acid mine drainage.

Mielke et al.[125] applied spaceborne hyperspectral and multispectral data to monitor mine waste mineralogy in south Africa. They derived iron feature depth (IFD) as a new index to detect the extend of waste minerals distribution. This index is justified with primary and secondary iron-bearing minerals. They performed material identification and characterization algorithm on the EO-1 Hyperion data for mineral identification. According to their results, integration

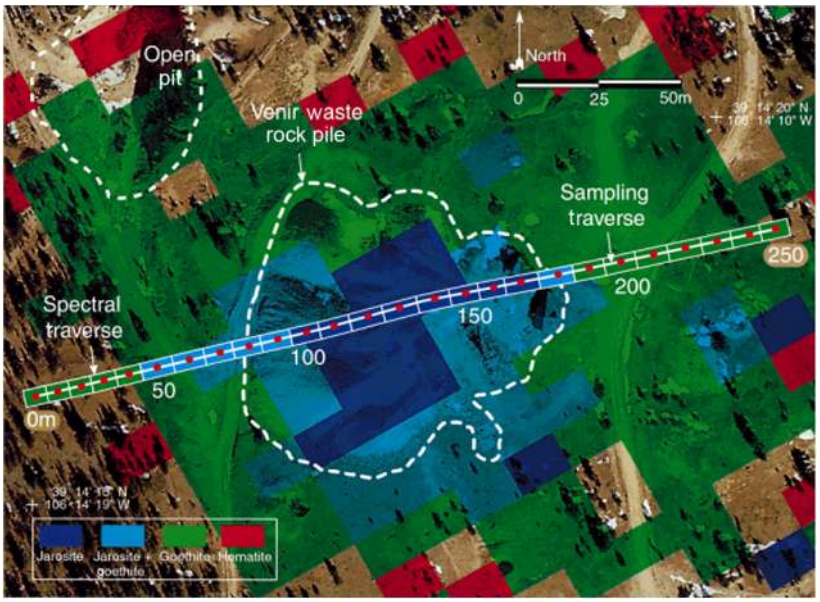

Fig. 12 Spectral traverse and AVIRIS mineral maps overlaid on a high-spatial-resolution aerial photograph of the Venir mine-waste pile. Mineral maps show the spectrally dominant Fe-bearing secondary minerals.[123]

of hyperspectral (EnMAP) and multispectral (Sentinel-2) for mineral mapping and IFD monitoring could be a promising proxy of mine waste.

7 Discussion and Conclusion

Although hyperspectral remote sensing data have been extensively used in different geologic fields such as lithological mapping, mineral exploration, and environmental geology in the last few decades, there are still several restrictions that limit the use of hyperspectral remote sensing in geological applications.

First, the availability of hyperspectral data is still very limited, and the available data only cover certain areas of the world. This has limited the scope of using hyperspectral remote sensing for geological applications. Although different airborne hyperspectral sensors (e.g., AVIRIS, HyMAP, HYDICE, and DAIS) and different spaceborne hyperspectral sensors (e.g., EO-1 Hyperion, EnMAP, HISUI, HyspIR, PRISMA, HYPXIM, MSMI, and HERO) have been developed, the number of hyperspectral sensors that are currently in use is very limited. Therefore, limited hyperspectral data are available with limited ground coverages.

Second, the spatial resolution (ground sampling distance or GSD) of the available spaceborne hyperspectral images, such as EO-1 Hyperion, is still limited. To improve the spatial resolution, the new spaceborne hyperspectral mission PRISMA added a panchromatic sensor with 5-m spatial resolution, and the forthcoming space-based HypXIM mission will add a 2-m panchromatic sensor. In addition, some researchers have attempted to combine spaceborne hyperspectral data with airborne hyperspectral images or with higher spatial resolution multispectral data (such as ASTER and Sentinel-2) to overcome the GSD limitation of spaceborne hyperspectral images.

Third, the SNR in the spectral bands of spaceborne hyperspectral images that are useful for geological applications is too low. For example, the SNR values of Hyperion spectral bands in VNIR region vary from 140:1 to 190:1, whereas their values are even lower in SWIR, 96:1 in 1.225 μm, 36:1 around 2.125 μm.[3] The most useful bands to detect minerals are around 2.0 to 2.4 μm (SWIR), whereas the bands around 0.43 to 0.90 μm are important for detecting ferric iron. According to Kruse et al.,[8] SNRs of at least 100:1 in the SWIR are required for mineral detection. Therefore, to improve the SNR, new spaceborne hyperspectral sensors have achieved a significant advancement. For example, the DESIS hyperspectral sensor has reached an SNR of ~200:1; but its GSD is still 30 m.[127] And the forthcoming hyperspectral sensors (i.e., PRISMA,

EnMAP, HISUI, SHALOM, HyspIRI, and HypXIM) are expected to have even higher SNR values in both the VNIR and the SWIR spectral ranges.[3] In addition, adjacent channel overlap and data redundancy are other issues about hyperspectral data.

According to the characteristics of hyperspectral data and the nature of geological information, the data processing approaches may differ from other conventional methods. Therefore, it is expected that special hyperspectral image processing techniques will be developed in the future to meet the requirements of geological applications.

Acknowledgments

This study was supported by the funding from the Canadian Space Agency's FAST (Flights and Fieldwork for the Advancement of Science and Technology) research grant (19FANBA36) received by the second author. We are grateful for the constructive comments provided by the editor and anonymous reviewers.

References

1. M. J. Abrams et al., "Mapping of hydrothermal alteration in the Cuprite mining district, Nevada, using aircraft scanner images for the spectral region 0.46 to 2.36 μm," *Geology* **5**(12), 713–8 (1977).
2. S.-E. Qian, *Hyperspectral Satellites and System Design*, CRC Press, Boca Raton (2020).
3. J. Transon et al., "Survey of hyperspectral Earth observation applications from space in the Sentinel-2 context," *Remote Sens.* **10**(2), 157 (2018).
4. B. Cooper et al., "Midinfrared spectral features of rocks and their powders," *J. Geophys. Res. Planets* **107**(E4), 1–17 (2002).
5. D. Green and M. Schodlok, "Characterisation of carbonate minerals from hyperspectral TIR scanning using features at 14 000 and 11 300 nm," *Aust. J. Earth Sci.* **63**(8), 951–957 (2016).
6. T. Kurz and S. Buckley, "A review of hyperspectral imaging in close range applications," *ISPRS Int. Arch. Photogramm. Remote Sens. Spat. Inf. Sci.* **XLI-B5**, 865–870 (2016).
7. F. D. Van der Meer et al., "Multi-and hyperspectral geologic remote sensing: a review," *Int. J. Appl. Earth Obs. Geoinf.* **14**(1), 112–128 (2012).
8. F. Kruse, J. Boardman, and J. Huntington, "Comparison of airborne hyperspectral data and EO-1 hyperion for mineral mapping," *IEEE Trans. Geosci. Remote Sens.* **41**, 1388–1400 (2003).
9. E. A. Cloutis, "Review article hyperspectral geological remote sensing: evaluation of analytical techniques," *Int. J. Remote Sens.* **17**(12), 2215–2242 (1996).
10. F. A. Kruse et al., "Mapping alteration minerals at prospect, outcrop and drill core scales using imaging spectrometry," *Int. J. Remote Sens.* **33**(6), 1780–1798 (2012).
11. S. Asadzadeh and C. R. de Souza Filho, "A review on spectral processing methods for geological remote sensing," *Int. J. Appl. Earth Obs. Geoinf.* **47**, 69–90 (2016).
12. D. Ramakrishnan and R. Bharti, "Hyperspectral remote sensing and geological applications," *Curr. Sci., Special Section: Hyperspectral Remote Sens.* **108**(5), 879–891 (2015).
13. E. Bedini, "The use of hyperspectral remote sensing for mineral exploration: a review," *J. Hyperspectral Remote Sens.* **7**(4), 189–211 (2017).
14. G. R. Hunt, "Spectral signatures of particulate minerals in the visible and near infrared," *Geophysics* **42**(3), 501–513 (1977).
15. R. N. Clark et al., "Imaging spectroscopy: earth and planetary remote sensing with the USGS Tetracorder and expert systems," *J. Geophys. Res. Planets* **108**(E12), 1 (2003).
16. D. Coulter et al., "Advances in spectral geology and remote sensing: 2008–2017," in *Proc. Exploration 17: Sixth Decennial Int. Conf. Mineral Exploration*, V. Tschirhart and M. D. Thomas, Eds., pp. 23–50 (2017).
17. A. B. Pour and M. Hashim, "ASTER, ALI and Hyperion sensors data for lithological mapping and ore minerals exploration," *Springerplus* **3**(1), 130 (2014).

18. R. N. Clark et al., "The US Geological Survey, Digital Spectral Reflectance Library: Version 1: 0.2 to 3.0 microns," U.S. Geological Survey Open File Report, 93-592 (1993).
19. R. N. Clark, "Spectroscopy of rocks and minerals, and principles of spectroscopy," in *Remote Sensing for the Earth Sciences: Manual of Remote Sensing*, 3rd ed., Vol. 3, A. N. Rencz, Ed., John Wiley & Sons, Inc., New York (1999).
20. J. W. Salisbury and N. Vergo, "*Infrared (2.1–25 um) spectra of minerals*," JCPDS International Centre for Diffraction Data, PA (1991).
21. J. B. Percival et al., "Customized spectral libraries for effective mineral exploration: mining National Mineral Collections," *Clays Clay Miner.* **66**(3), 297–314 (2018).
22. A. F. Goetz, B. Curtiss, and D. A. Shiley, "Rapid gangue mineral concentration measurement over conveyors by NIR reflectance spectroscopy," *Miner. Eng.* **22**(5), 490–499 (2009).
23. F. A. Kruse, "Advances in hyperspectral remote sensing for geologic mapping and exploration," in *Proc. 9th Aust. Remote Sens. Conf.* (1998).
24. P. Shippert, "Why use hyperspectral imagery?" *Photogramm. Eng. Remote Sens.* **70**(4), 377–396 (2004).
25. K. V. Kale et al., "A research review on hyperspectral data processing and analysis algorithms," *Proc. Natl. Acad. Sci. India Sect. A* **87**(4), 541–55 (2017).
26. B.-C. Gao et al., "Atmospheric correction algorithms for hyperspectral remote sensing data of land and ocean," *Remote Sens. Environ.* **113**, S17–S24 (2009).
27. F. A. Kruse, "Mineral mapping with AVIRIS and EO-1 hyperion" (2004).
28. S. Minu, A. Shetty, and B. Gopal, "Review of preprocessing techniques used in soil property prediction from hyperspectral data," *Cogent Geosci.* **2**(1), 1145878 (2016).
29. D. A. Roberts, Y. Yamaguchi, and R. J. P. Lyon, "Comparison of various techniques for calibration of AIS data," *JPL Proc. 2nd Airborn Imaging Spectrometer Data Anal. Workshop*, pp. 21–30 (1986).
30. J. E. Conel et al., "AIS-2 radiometry and a comparison of methods for the recovery of ground reflectance," Airborne Imaging Spectrometer Data Analysis Workshop (1987).
31. P. N. Reinersman, K. L. Carder, and F.-I. R. Chen, "Satellite-sensor calibration verification with the cloud-shadow method," *Appl. Opt.* **37**(24), 5541–9 (1998).
32. L. S. Bernstein et al., "Validation of the quick atmospheric correction (QUAC) algorithm for VNIR-SWIR multi-and hyperspectral imagery," *Proc. SPIE* **5806**, 668–678 (2005).
33. A. F. Goetz et al., "Imaging spectrometry for earth remote sensing," *Science* **228**(4704), 1147–1153 (1985).
34. E. Ben-Dor, B. Kindel, and A. Goetz, "Quality assessment of several methods to recover surface reflectance using synthetic imaging spectroscopy data," *Remote Sens. Environ.* **90**(3), 389–404 (2004).
35. B.-C. Gao, K. B. Heidebrecht, and A. F. Goetz, "Derivation of scaled surface reflectances from AVIRIS data," *Remote Sens. Environ.* **44**(2-3), 165–178 (1993).
36. R. Richter, "Atmospheric correction of DAIS hyperspectral image data," *Comput. Geosci.* **22**(7), 785–793 (1996).
37. S. M. Adler-Golden et al., "Atmospheric correction for shortwave spectral imagery based on MODTRAN4," *Proc. SPIE* **3753**, 61–69 (1999).
38. K. Staenz, T. Szeredi, and J. Schwarz, "ISDAS—a system for processing/analyzing hyperspectral data," *Can. J. Remote Sens.* **24**(2), 99–113 (1998).
39. Z. Qu, B. C. Kindel, and A. F. Goetz, "The high accuracy atmospheric correction for hyperspectral data (HATCH) model," *IEEE Trans. Geosci. Remote Sens.* **41**(6), 1223–1231 (2003).
40. A. Agarwal et al., "Efficient hierarchical-PCA dimension reduction for hyperspectral imagery," in *IEEE Int. Symp. Signal Process. and Inf. Technol.*, IEEE (2007).
41. G. Luo et al., "Minimum noise fraction versus principal component analysis as a preprocessing step for hyperspectral imagery denoising," *Can. J. Remote Sens.* **42**(2), 106–116 (2016).
42. R. Rajagopal and V. Ranganathan, "Evaluation of effect of unsupervised dimensionality reduction techniques on automated arrhythmia classification," *Biomed. Signal Process. Control* **34**, 1–8 (2017).

43. A. Hyvärinen, "Independent component analysis: recent advances," *Philos. Trans. R. Soc., A* **371**(1984), 20110534 (2013).
44. L. Zhang et al., "Dimensionality reduction based on clonal selection for hyperspectral imagery," *IEEE Trans. Geosci. Remote Sens.* **45**(12), 4172–4186 (2007).
45. T. Zhang, D. Tao, and J. Yang, "Discriminative locality alignment," *Lect. Notes Comput. Sci.* **5302**, 725–738 (2008).
46. W. Li et al., "Locality-preserving dimensionality reduction and classification for hyperspectral image analysis," *IEEE Trans. Geosci. Remote Sens.* **50**(4), 1185–1198 (2012).
47. N. H. Ly, Q. Du, and J. E. Fowler, "Sparse graph-based discriminant analysis for hyperspectral imagery," *IEEE Trans. Geosci. Remote Sens.* **52**(7), 3872–3884 (2014).
48. L. Zhang et al., "Ensemble manifold regularized sparse low-rank approximation for multiview feature embedding," *Pattern Recognit.* **48**(10), 3102–3112 (2015).
49. N. Shental et al., "Adjustment learning and relevant component analysis," *Lect. Notes Comput. Sci.* **2353**, 776–790 (2002).
50. J. Goldberger et al., "Neighbourhood components analysis," in *Advances in Neural Inf. Process. Syst.*, Vol. 17, pp. 513–20 (2004).
51. J. V. Davis et al., "Information-theoretic metric learning," in *Proc. 24th Int. Conf. Mach. Learn.* (2007).
52. Y. Dong et al., "Dimensionality reduction and classification of hyperspectral images using ensemble discriminative local metric learning," *IEEE Trans. Geosci. Remote Sens.* **55**(5), 2509–2524 (2017).
53. S. T. Roweis and L. K. Saul, "Nonlinear dimensionality reduction by locally linear embedding," *Science* **290**(5500), 2323–2326 (2000).
54. C. Chen et al., "Constrained Laplacian eigenmap for dimensionality reduction," *Neurocomputing* **73**(4-6), 951–958 (2010).
55. C. M. Bachmann, T. L. Ainsworth, and R. A. Fusina, "Exploiting manifold geometry in hyperspectral imagery," *IEEE Trans. Geosci. Remote Sens.* **43**(3), 441–454 (2005).
56. X. He et al., "Neighborhood preserving embedding," in *Tenth IEEE Int. Conf. Comput. Vision*, Vol. 1, IEEE (2005).
57. H. Huang, M. Chen, and Y. Duan, "Dimensionality reduction of hyperspectral image using spatial-spectral regularized sparse hypergraph embedding," *Remote Sensing* **11**(9), 1039 (2019).
58. W. Du et al., "Semi-supervised dimension reduction based on hypergraph embedding for hyperspectral images," *Int. J. Remote Sens.* **39**(6), 1696–1712 (2018).
59. Y. Zhou, J. Peng, and C. P. Chen, "Dimension reduction using spatial and spectral regularized local discriminant embedding for hyperspectral image classification," *IEEE Trans. Geosci. Remote Sens.* **53**(2), 1082–1095 (2015).
60. F. Kowkabi, H. Ghassemian, and A. Keshavarz, "A fast spatial–spectral preprocessing module for hyperspectral endmember extraction," *IEEE Geosci. Remote Sens. Lett.* **13**(6), 782–786 (2016).
61. A. Plaza et al., "A quantitative and comparative analysis of endmember extraction algorithms from hyperspectral data," *IEEE Trans. Geosci. Remote Sens.* **42**(3), 650–663 (2004).
62. D. C. Heinz and I. C. Chein, "Fully constrained least squares linear spectral mixture analysis method for material quantification in hyperspectral imagery," *IEEE Trans. Geosci. Remote Sens.* **39**(3), 529–545 (2001).
63. M. Parente and A. Plaza, "Survey of geometric and statistical unmixing algorithms for hyperspectral images," *in 2nd Workshop Hyperspectral Image and Signal Process.: Evol. Remote Sens.*, IEEE (2010).
64. K. Wu et al., "A novel endmember extraction method using sparse component analysis for hyperspectral remote sensing imagery," *IEEE Access* **6**, 75206–75215 (2018).
65. T. Nouri, M. M. Oskouei, and H. Zekri, "A comparison study of ORASIS and VCA for mineralogical unmixing of hyperspectral data," *J. Indian Soc. Remote Sens.* **44**(5), 723–733 (2016).
66. C.-I. Chang, *Hyperspectral Data Exploitation: Theory and Applications*, John Wiley & Sons, Hoboken, New Jersey (2007).

67. L. Miao and H. Qi, "Endmember extraction from highly mixed data using minimum volume constrained nonnegative matrix factorization," *IEEE Trans. Geosci. Remote Sens.* **45**(3), 765 (2007).
68. T. Nouri et al., "Improvement of the MVC-NMF problem using particle swarm optimization for mineralogical unmixing of noisy hyperspectral data," *J. Indian Soc. Remote Sens.* **47**(4), 541–550 (2019).
69. J. Li and J. M. Bioucas-Dias, "Minimum volume simplex analysis: a fast algorithm to unmix hyperspectral data," in *IEEE Int. Geosci. and Remote Sens. Symp.* (2008).
70. J. Li et al., "Minimum volume simplex analysis: a fast algorithm for linear hyperspectral unmixing," *IEEE Trans. Geosci. Remote Sens.* **53**(9), 5067–5082 (2015).
71. T.-H. Chan et al., "A convex analysis-based minimum-volume enclosing simplex algorithm for hyperspectral unmixing," *IEEE Trans. Signal Process.* **57**(11), 4418–4432 (2009).
72. M. D. Craig, "Minimum-volume transforms for remotely sensed data," *IEEE Trans. Geosci. Remote Sens.* **32**(3), 542–552 (1994).
73. J. Broadwater, A. Banerjee, and P. Burlina, "Kernel methods for unmixing hyperspectral imagery," in *Kernel Methods for Remote Sensing Data Analysis*, pp. 249–70 (2009).
74. R. Heylen, D. Burazerovic, and P. Scheunders, "Non-linear spectral unmixing by geodesic simplex volume maximization," *IEEE J. Sel. Top. Signal Process.* **5**(3), 534–542 (2011).
75. M. T. Eismann and R. C. Hardie, "Stochastic spectral unmixing with enhanced endmember class separation," *Appl. Opt.* **43**(36), 6596–608 (2004).
76. D. Lu and Q. Weng, "A survey of image classification methods and techniques for improving classification performance," *Int. J. Remote Sens.* **28**(5), 823–870 (2007).
77. M. Pal, T. Rasmussen, and A. Porwal, "Optimized lithological mapping from multispectral and hyperspectral remote sensing images using fused multi-classifiers," *Remote Sensing* **12**(1), 177 (2020).
78. D. Chutia et al., "Hyperspectral remote sensing classifications: a perspective survey," *Trans. GIS* **20**(4), 463–490 (2016).
79. S. Amini, S. Homayouni, and A. Safari, "Semi-supervised classification of hyperspectral image using random forest algorithm," in *IEEE Geosci. and Remote Sens. Symp.*, IEEE (2014).
80. R. Heylen, M. Parente, and P. Gader, "A review of nonlinear hyperspectral unmixing methods," *IEEE J. Sel. Top. Appl. Earth Obs. Remote Sens.* **7**(6), 1844–1868 (2014).
81. S. S. Nath et al., "A survey of image classification methods and techniques," in *Int. Conf. Control, Instrum., Commun. and Comput. Technol.*, IEEE (2014).
82. J. F. Mustard and J. M. Sunshine, "Spectral analysis for earth science: investigations using remote sensing data," in *Remote Sensing for the Earth Sciences: Manual of Remote Sensing*, A. N. Rencz, Ed., Vol. 3, pp. 251–307, John Wiley & Sons, Inc, New York (1999).
83. F. van der Meer, "Analysis of spectral absorption features in hyperspectral imagery," *Int. J. Appl. Earth Obs. Geoinf.* **5**(1), 55–68 (2004).
84. J. A. Richards and X. Jia, "Interpretation of hyperspectral image data," in *Remote Sensing Digital Image Analysis: An Introduction*, J. D. Richards and X. Jia, Eds., pp. 359–88, Springer, Berlin, Heidelberg(2006).
85. C. Kumar et al., "Automated lithological mapping by integrating spectral enhancement techniques and machine learning algorithms using AVIRIS-NG hyperspectral data in Gold-bearing granite-greenstone rocks in Hutti, India," *Int. J. Appl. Earth Obs. Geoinf.* **86**, 102006 (2020).
86. S. Salehi, C. Mielke, and C. Rogass, "Mapping ultramafic complexes using airborne imaging spectroscopy and spaceborne data in Arctic regions with abundant lichen cover, a case study from the Niaqornarssuit complex in South West Greenland," *Eur. J. Remote Sens.* **53**(1), 156–175 (2020).
87. J. Harris et al., "Mapping lithology in Canada's Arctic: application of hyperspectral data using the minimum noise fraction transformation and matched filtering," *Can. J. Earth Sci.* **42**(12), 2173–2193 (2005).
88. X. Zhang and P. Li, "Lithological mapping from hyperspectral data by improved use of spectral angle mapper," *Int. J. Appl. Earth Obs. Geoinf.* **31**, 95–109 (2014).
89. A. Dadon et al., "Examination of spaceborne imaging spectroscopy data utility for stratigraphic and lithologic mapping," *J. Appl. Remote Sens.* **5**(1), 053507 (2011).

90. J. F. Huntington, "The role of remote sensing in finding hydrothermal mineral deposits on earth," *Ciba Found Symp.* **202**, 214–31 (1996).
91. R. Sillitoe, "Porphyry copper systems," *Econ. Geol.* **105**, 3–41 (2010).
92. X. Zhou et al., "Multi-scale integrated application of spectral geology and remote sensing for mineral exploration," in *Proc. 6th Decennial Int. Conf. Mineral Exploration*, Toronto, ON (2017).
93. F. Pirajno, "A classification of mineral systems, overviews of plate tectonic margins and examples of ore deposits associated with convergent margins," *Gondwana Res.* **33**, 44–62 (2016).
94. L. Liu et al., "Mapping alteration using imagery from the Tiangong-1 hyperspectral spaceborne system: example for the Jintanzi gold province, China," *Int. J. Appl. Earth Obs. Geoinf.* **59**, 31–41 (2017).
95. D. A. John et al., "Descriptive models for epithermal gold-silver deposits: chapter Q in mineral deposit models for resource assessment," Report No.: 2328-0328, US Geological Survey (2018).
96. A. Crosta et al., "Targeting key alteration minerals in epithermal deposits in Patagonia, Argentina, using ASTER imagery and principal component analysis," *Int. J. Remote Sens.* **24**(21), 4233–40 (2003).
97. F. van der Meer et al., "Wavelength feature mapping as a proxy to mineral chemistry for investigating geologic systems: an example from the Rodalquilar epithermal system," *Int. J. Appl. Earth Obs. Geoinf.* **64**, 237–248 (2018).
98. O. Corumluoglu, A. Vural, and I. Asri, "Determination of Kula basalts (geosite) in Turkey using remote sensing techniques," *Arabian J. Geosci.* **8**(11), 10105–10117 (2015).
99. A. Vural, Ö. Corumluoglu, and I. Asri, "Remote sensing technique for capturing and exploration of mineral deposit sites in Gumushane metallogenic province, NE Turkey," *J. Geol. Soc. India* **90**(5), 628–633 (2017).
100. R. A. Ayuso et al., "Porphyry copper deposit model: chapter B in mineral deposit models for resource assessment," Report No.: 2328-0328, US Geological Survey (2010).
101. S. Halley, J. Dilles, and R. Tosdal, "Footprints: the hydrothermal alteration and geochemical dispersion around porphyry copper deposits," *Society of Economic Geologists Newsletter* **100**(1), 12–17 (2015).
102. C. A. Bishop, J. G. Liu, and P. J. Mason, "Hyperspectral remote sensing for mineral exploration in Pulang, Yunnan province, China," *Int. J. Remote Sens.* **32**(9), 2409–2426 (2011).
103. G. E. Graham et al., "Application of imaging spectroscopy for mineral exploration in Alaska: a study over porphyry Cu deposits in the eastern Alaska Range," *Econ. Geol.* **113**(2), 489–510 (2018).
104. M. H. Zadeh et al., "Sub-pixel mineral mapping of a porphyry copper belt using EO-1 Hyperion data," *Adv. Space Res.* **53**(3), 440–451 (2014).
105. M. D. Barton, *Iron Oxide (-Cu-Au-REE-P-Ag-U-Co) Systems. Treatise on Geochemistry*, 2nd ed., pp. 515–41, Elsevier Inc, San Diego (2013).
106. L. Corriveau et al., "Alteration vectoring to IOCG (U) deposits in frontier volcano-plutonic terrains, Canada," in *Proc. Exploration* (2007).
107. M. C. Tappert et al., "The mineral chemistry, near-infrared, and mid-infrared reflectance spectroscopy of phengite from the Olympic Dam IOCG deposit, South Australia," *Ore Geol. Rev.* **53**, 26–38 (2013).
108. C. Laukamp et al., "Hydrothermal mineral alteration patterns in the Mount Isa Inlier revealed by airborne hyperspectral data," *Aust. J. Earth Sci.* **58**(8), 917–936 (2011).
109. W. P. Shanks, III et al., "Volcanogenic massive sulfide occurrence model: chapter C in mineral deposit models for resource assessment," Report No.: 2328-0328, US Geological Survey (2012).
110. A.-L. Bonnet and L. Corriveau, "Alteration vectors to metamorphosed hydrothermal systems in gneissic terranes," in *Mineral Deposits of Canada: A Synthesis of Major Deposit-Types, District Metallogeny, the Evolution of Geological Provinces, and Exploration Methods*, W. D. Goodfellow, Eds., Vol. 5, pp. 1035–49, Geological Association of Canada, Mineral Deposits Division, Special Publication (2007).

111. F. J. van Ruitenbeek et al., "Characterization of the hydrothermal systems associated with Archean VMS-mineralization at Panorama, Western Australia, using hyperspectral, geochemical and geothermometric data," *Ore Geol. Rev.* **45**, 33–46 (2012).
112. P. Samani, S. Prizomwala, and A. Rajawat, "Assessing the mineral alteration in Ambaji–Deri Region (Northwestern India) using hyperspectral remote sensing," *J. Indian Soc. Remote Sens.* **49**, 249–257 (2020).
113. K. Laakso et al., "Application of airborne, laboratory, and field hyperspectral methods to mineral exploration in the Canadian Arctic: recognition and characterization of volcanogenic massive sulfide-associated hydrothermal alteration in the Izok Lake deposit area, Nunavut, Canada," *Econ. Geol.* **110**(4), 925–941 (2015).
114. L. D. Meinert, "Skarns and skarn deposits," *Geosci. Canada* **19**(4), 145–162 (1992).
115. Y. Xu, J. Chen, and P. Meng, "Detection of alteration zones using hyperspectral remote sensing data from Dapingliang skarn copper deposit and its surrounding area, Shanshan county, Xinjiang Uygur autonomous region, China," *J. Vis. Commun. Image Represent.* **58**, 67–78 (2019).
116. J. Tian et al., "Short wavelength infra-red (SWIR) characteristics of hydrothermal alteration minerals in skarn deposits: example from the Jiguanzui Cu–Au deposit, Eastern China," *Ore Geol. Rev.* **106**, 134–149 (2019).
117. B. Dkhala et al., "Hyperspectral field spectroscopy and Sentinel-2 multispectral data for minerals with high pollution potential content estimation and mapping," *Sci. Total Environ.* **740**, 140160 (2020).
118. S. Abbasi et al., "Bioaccessibility of barium from barite contaminated soils based on gastric phase in vitro data and plant uptake," *Chemosphere* **144**, 1421–1427 (2016).
119. X. Yang et al., "Use of hyperspectral imagery to detect affected vegetation and heavy metal polluted areas: a coal mining area, China," *Geocarto Int.* 1–20 (2020).
120. A. Riaza et al., "Mapping acidic water in an acid mine drainage-contaminated river with hyperspectral airborne hymap data," Odiel River, SW Spain (2012).
121. C. Ehrler, C. Fischer, and M. Bachmann, "Hyperspectral Remote Sensing Applications in Mining Impact Analysis," in *34th Int. Symp. Remote Sens. Environ.* (2011).
122. E. Choe et al., "Mapping of heavy metal pollution in stream sediments using combined geochemistry, field spectroscopy, and hyperspectral remote sensing: a case study of the Rodalquilar mining area, SE Spain," *Remote Sens. Environ.* **112**(7), 3222–3233 (2008).
123. G. A. Swayze et al., "Using imaging spectroscopy to map acidic mine waste," *Environ. Sci. Technol.* **34**(1), 47–54 (2000).
124. S. Raval, R. Merton, and D. Laurence, "Mine tailings water mapping using CHRIS Proba imagery," *in 4th Workshop Hyperspectral Image and Signal Process.: Evol. Remote Sens.*, IEEE (2012).
125. C. Mielke et al., "Spaceborne mine waste mineralogy monitoring in South Africa, applications for modern push-broom missions: hyperion/OLI and EnMAP/Sentinel-2," *Remote Sens.* **6**(8), 6790–6816 (2014).
126. G. E. Davies and W. M. Calvin, "Mapping acidic mine waste with seasonal airborne hyperspectral imagery at varying spatial scales," *Environ. Earth Sci.* **76**, 432 (2017).
127. B. E. Teledyne, "DESIS: frequently asked questions," https://tbecom/geospatial/faq-DESIS.

Sima Peyghambari received her PhD in geology (petrology) from Shahid Bahonar University of Kerman. She is an assistant professor in Geology Department of Payame-Noor University of Tehran. She is Master of Science student in Engineering under supervising of Dr. Zhang at University of New Brunswick. She has authored or coauthored over 10 research papers.

Yun Zhang received his PhD from the Free University of Berlin. He is a fellow of Canadian Academy of Engineering (FCAE), and a professor in remote sensing at the University of New Brunswick, Canada. He has authored or coauthored over 260 research papers. The research outcomes from his lab have resulted 15 patents, 3 new patent applications, and more than ten technology licenses. In addition, he received many prestigious national and international research awards.